Journal of
Sensor and Actuator Networks

MDPI

Article

An Integrated Framework for Anomaly Detection in Photovoltaic Systems Using UAV Multi-Sensor Data and SCADA Telemetry

Teodor Lupoiu [1,2], Constantin Ionescu [1], Anatoli Paul Ulmeanu [1], Horia Necula [1], Grigore Cican [2,3] and Lucian Teodor Grigorie [4,*]

[1] Faculty of Energy Engineering, National University of Science and Technology Politehnica Bucharest, 313 Splaiul Independentei, Sector 6, EI 101 Building, 060042 Bucharest, Romania; teodor.lupoiu@upb.ro (T.L.); ionescu.constantin@upb.ro (C.I.); paul.ulmeanu@upb.ro (A.P.U.); horia.necula@upb.ro (H.N.)
[2] CAMPUS Research Institute, National University of Science and Technology Politehnica Bucharest, Splaiul Independenţei No. 313, Sector 6, 060042 Bucharest, Romania
[3] Romania National Research and Development Institute for Gas Turbines COMOTI, 220D Iuliu Maniu, 061126 Bucharest, Romania
[4] Faculty of Aerospace Engineering, National University of Science and Technology Politehnica Bucharest, 1–7 Polizu Street, 1, 011061 Bucharest, Romania
* Correspondence: teodor.grigorie@upb.ro

Abstract

This study proposes an integrated framework for photovoltaic (PV) anomaly diagnosis combining unmanned aerial vehicle (UAV) radiometric thermography and red–green–blue (RGB) imagery, supervisory control and data acquisition (SCADA) telemetry, meteorological measurements, solar-shading modelling, automated defect detection, and ground-level verification. The methodology was evaluated on a 26.73 kWp rooftop PV installation comprising 81 modules using 77 producing days and 3543 valid 30 min observations. UAV thermography identified an open-circuited string and shading-induced hotspots, with peak hotspot temperatures reaching 109.9 °C and temperature differences exceeding 60 °C relative to the surrounding module surface. Radiometric analysis showed uniform temperature elevations of up to 5.3 K for the open-circuited string. To isolate maintenance effects from meteorological variability, 376 pre- and post-intervention intervals were matched according to irradiance, ambient temperature, relative humidity, and wind speed. The analysis yielded a mean power increase of 0.518 kW (95% confidence interval: 0.321–0.714 kW), corresponding to 28.3% relative to the matched pre-intervention mean. Two of the four anomaly classes considered occurred on the installation (one open-circuited string and 14 shading-induced hotspot regions). Within the limits of this single-installation case study, the framework enabled thermal anomaly detection, root-cause discrimination, and quantitative assessment of PV performance changes, supporting condition-based maintenance and operational decision-making.

Keywords: photovoltaic systems; UAV thermography; anomaly detection; SCADA telemetry; infrared thermography; fault diagnosis; predictive maintenance; hotspot detection; open-circuit fault; solar shading

Check for updates

Academic Editor: Lei Shu

Received: 20 August 2026
Revised: 2 October 2026
Accepted: 20 October 2026
Published: 22 October 2026

Copyright: © 2026 by the authors. Licensee MDPI, Basel, Switzerland. This article is an open access article distributed under the terms and conditions of the Creative Commons Attribution (CC BY) license.

1. Introduction

Few technologies have transformed the global energy landscape as rapidly as solar photovoltaics (PV). Driven by technological innovation, declining manufacturing costs, and increasingly ambitious decarbonization policies, PV has become one of the fastest-growing

electricity generation technologies worldwide [1]. In 2022, cumulative installed PV capacity exceeded one terawatt-peak (TWp) for the first time, while only two years later global installations surpassed 2.2 TWp [2]. Current projections indicate that worldwide capacity will approach 3 TWp by the end of 2025, with the European Union expected to increase its installed capacity from 347 GWp in 2024 to approximately 700–750 GWp by 2030 [1,3]. At the same time, commercial PV module efficiencies have increased from approximately 9% in 1980 to more than 22% today, while emerging tandem silicon–perovskite technologies have demonstrated conversion efficiencies exceeding 30% under laboratory conditions [4,5]. These developments have been accompanied by an approximately 87% reduction in the levelized cost of electricity since 2010 [6].

The rapid expansion of PV installations has shifted research priorities from maximizing conversion efficiency toward ensuring long-term operational reliability. PV power plants are expected to operate for more than 25 years under variable environmental conditions, making preservation of their electrical performance an important technical and economic objective [7,8]. A recent meta-analysis of 80 studies comprising more than 600 degradation-rate observations reported a median degradation rate of 0.94% per year and a mean value of 1.1% per year, identifying climatic conditions, installation configuration, and PV technology among the dominant influencing factors [7,9]. PV modules are continuously exposed to ultraviolet (UV) radiation, humidity, thermal cycling, mechanical loading, wind, and high system voltages, which can initiate degradation mechanisms affecting both encapsulation materials and photovoltaic cells [7,10]. Typical manifestations include delamination, corrosion, solder fatigue, microcracking, hotspot formation, and potential-induced degradation (PID), resulting in power loss, accelerated ageing, and potentially safety hazards [7,11]. Consequently, early detection of these mechanisms is essential for predictive maintenance and for minimizing long-term energy losses [12,13].

The increasing size and complexity of PV installations also creates significant inspection and maintenance challenges. Utility-scale plants may contain hundreds of thousands of interconnected modules, making conventional ground-based inspections slow, labour-intensive, and costly [14,15]. Furthermore, inverter and monitoring measurements can indicate a reduction in system performance without necessarily identifying the precise location or physical origin of the fault [12,16]. Non-contact diagnostic techniques capable of rapidly surveying complete PV installations have therefore become increasingly important for condition monitoring and asset management [17,18].

Among these techniques, infrared thermography is widely used to evaluate PV modules under operating conditions [17,19]. Electrical faults and degradation mechanisms modify current distribution within photovoltaic cells and can generate characteristic thermal anomalies [20]. Depending on their origin, these anomalies may appear as localized hotspots, overheated substrings associated with bypass-diode activation, edge heating related to PID, uniformly overheated modules resulting from open-circuit conditions, or irregular temperature distributions caused by soiling, vegetation, and partial shading [17]. Because thermal abnormalities may become observable before substantial electrical performance degradation is detected, infrared thermography provides an effective means of identifying potentially defective modules at an early stage [12,18].

The development of unmanned aerial vehicles (UAVs) [21] has considerably expanded the practical application of infrared thermography to PV diagnostics. UAV-mounted radiometric cameras enable rapid acquisition of high-resolution thermal and visible imagery over large installations, reducing inspection time compared with conventional handheld surveys [17]. Modern platforms combine thermal infrared sensors, high-resolution red–green–blue (RGB) cameras, and global navigation satellite system (GNSS) positioning, allowing detected anomalies to be georeferenced and documented [15]. Recent develop-

ments in computer vision and deep learning have further automated module detection and thermal-anomaly classification from aerial imagery [22,23].

Despite these advances, most published UAV-based studies remain focused primarily on automatic detection, classification, and localization of thermal anomalies [24,25]. Machine- and deep-learning approaches have demonstrated high performance in identifying hotspots, bypass-diode activation, PID, soiling, and other defects, but comparatively few investigations relate these observations directly to the electrical behaviour of the PV installation [26,27]. Thermographic inspections therefore frequently remain qualitative, identifying the existence and location of an anomaly without quantifying its effect on electrical production or verifying its physical origin through complementary measurements [28]. Similarly, limited attention has been devoted to jointly exploiting aerial thermography, supervisory control and data acquisition (SCADA) data, meteorological observations, and electrical verification to distinguish permanent degradation from temporary environmental effects [29,30].

Integrating UAV thermography with SCADA operational data can provide a more comprehensive assessment of PV system health. Aerial imagery offers high spatial resolution for fault localization, whereas SCADA systems continuously record electrical parameters such as voltage, current, power output, inverter performance, and energy yield [31,32]. When these measurements are interpreted together with meteorological information, thermal anomalies can be assessed under their actual operating conditions, reducing false-positive diagnoses caused by transient irradiance variations, shading, or changing environmental conditions. Furthermore, comparison of electrical performance before and after maintenance can provide quantitative evidence of the effectiveness of corrective actions [29].

Recent studies illustrate the substantial progress achieved in automated aerial PV inspection. Wang et al. [33] proposed an online anomaly-detection framework based on aerial thermography and low-rank matrix decomposition, demonstrating the feasibility of automated processing of thermal video streams. de Oliveira AKV et al. [34] reported that modern deep-learning approaches can achieve classification accuracies exceeding 90%, while module detection and segmentation methods have reached F1-scores of up to 98.4%, although fully autonomous workflows and tighter integration with plant monitoring remain important challenges.

Bommes et al. [35] developed a computer-vision framework for semi-automatic processing of UAV thermal videos using a dataset containing 4.3 million infrared images of 107,842 PV modules from seven plants. Their ResNet-50 classifier achieved more than 90% test accuracy for ten anomaly classes, while the extraction algorithm enabled inspection rates between 3.5 and 9 MWp per day. In subsequent work, a supervised contrastive learning framework trained on 2.92 million infrared images achieved area under the receiver operating characteristic curve (AUROC) values ranging from 73.3% to 96.6% under different source–target combinations and correctly classified 79.4% of normal and 77.1% of anomalous module images using a fixed decision threshold [23]. To address fault localization, a Structure-from-Motion-based framework subsequently georeferenced 99.3% of 35,084 modules and automatically extracted more than 2.2 million module images [36].

Field studies have likewise demonstrated the practical effectiveness of aerial thermography. Grimaccia et al. [37] identified common operating faults, including hotspots, disconnected cells, and bypass-diode failures, during UAV-based operation and maintenance campaigns on PV plants in Italy. Gallardo-Saavedra et al. [17] emphasized the influence of camera resolution, flight altitude, spatial resolution, and environmental conditions on defect detectability and concluded that aerial thermography represents a rapid and cost-effective alternative to conventional inspections. Di Tommaso et al. [38] proposed a

multi-stage framework based on You Only Look Once version 3 (YOLOv3) processing both infrared and visible UAV imagery, achieving an average precision (AP@0.5) above 98% for PV panel detection, approximately 88.3% AP@0.4 for hotspot detection, and approximately 70% mean average precision (mAP@0.5) for visible-spectrum defect detection, with an average inference time of 0.98 s per image.

Although these studies demonstrate substantial progress in automated UAV inspection, the majority focus on defect detection, classification, and localization rather than establishing quantitative relationships between thermographic abnormalities and plant-level electrical performance. This limitation is particularly relevant when thermal signatures may originate from transient environmental effects rather than permanent electrical degradation. Muttillo et al. [39], for example, investigated 12 defective PV modules by combining infrared thermography with electrical modelling and current–voltage (I–V) characteristics, demonstrating that specific thermal patterns can be related to reductions in module efficiency and power output. Such studies indicate the value of thermal–electrical correlation but also highlight the need for integrated diagnostic workflows that combine spatial, electrical, and environmental information.

More recent data-driven contributions have advanced along two largely separate lines. On the electrical side, Amiri et al. [40] trained random forest classifiers on maximum-power-point data simulated with an experimentally calibrated one-diode model of the array, using one binary classifier for fault detection and one multiclass classifier for fault diagnosis, and reported an accuracy of 99.4% for faults such as short circuits, line-to-line faults, open circuits, and shading, outperforming several other supervised classifiers, including support vector machine and k-nearest neighbour models. On the imaging side, Peng et al. [41] derived a lightweight oriented-bounding-box detector from YOLOv8 to extract PV arrays from UAV infrared images, reaching 99.1% mAP@0.5 at approximately 60 frames per second with 8.52 million parameters; hotspots, diode failures, and obstructions were then identified with accuracies of 96.97%, 100%, and 88.89%, respectively, and GNSS metadata, the Hough transform, and K-means clustering returned the row–column index of each defective module. The authors note, however, that thermal reflections are not distinguished from genuine hotspots and that the thresholds depend on the acquisition protocol. Both approaches draw on a single data source, require labelled or simulated training data, and deliver a class label or a bounding box whose quality is expressed as classification or detection accuracy. The present framework differs in purpose and in structure: it does not introduce a new classifier, and the learned detector is retained only as a screening stage. Its output is tested against evidence that does not depend on it (per-module radiometric comparison, cast-shadow simulation, RGB imagery, and region-level SCADA records), and the diagnosis is closed by field electrical measurement. The outcome is a verified root cause and a measured change in electrical output rather than a predicted label.

To address this research gap, this study proposes an integrated framework for PV anomaly assessment combining UAV-based radiometric infrared thermography, high-resolution RGB imagery, SCADA operational measurements, local meteorological observations, spatial irradiance and shading modelling, automated anomaly detection, and targeted field electrical verification. Unlike conventional UAV inspection approaches focused primarily on defect identification, the proposed methodology follows the complete diagnostic chain from aerial anomaly detection and environmental discrimination to root-cause verification and quantitative assessment of electrical performance. The framework is evaluated through pre- and post-intervention investigations of a rooftop PV installation located at the National University of Science and Technology POLITEHNICA Bucharest, with the aim of improving fault diagnosis, supporting maintenance prioritization, and providing objective evidence of the performance benefits associated with targeted corrective

actions. Throughout the paper, anomaly diagnosis denotes a four-level process comprising (i) detection and localization, (ii) fault-type identification and root-cause attribution, (iii) severity quantification, and (iv) maintenance decision support; prognosis of future degradation lies outside its scope.

The novelty of the work lies in combining the components listed above into a single verifiable workflow and in measuring, rather than assuming, the outcome of the corrective intervention. The main contributions are summarized as follows:

- An end-to-end diagnostic framework linking UAV radiometric thermography and RGB imagery with SCADA telemetry, on-site meteorological measurements, solar-shading modelling based on a digital surface model (DSM), automated defect detection, and ground-level electrical verification. In contrast to the detection-, classification-, and localization-oriented studies reviewed above [33–38,40,41], the workflow extends from aerial anomaly detection to a confirmed root cause and a measured electrical consequence.
- A physics-based procedure for separating transient shading-induced hotspots from intrinsic module defects, in which the r.sun solar radiation model is run over a DSM reconstructed from the same UAV survey to simulate the cast-shadow geometry at the timestamp of each thermographic acquisition. In the case study, all 14 detected hotspot regions (peak temperature 109.9 °C) were attributed to vegetation shading and confirmed by ground thermography, so that vegetation clearance rather than module replacement was identified as the appropriate corrective action.
- A detection architecture in which the deep-learning detector acts as a screening stage rather than as the basis for maintenance decisions. Two paths that are independent of the detector, namely a per-module radiometric median comparison (which isolated the open-circuited string through a uniform temperature elevation of up to 5.3 K) and a per-region SCADA analysis, limit the exposure to false negatives, and the consequences and cost drivers of both error types are analysed explicitly.
- A weather-matched paired analysis that quantifies the effect of maintenance from routine SCADA data. Pre- and post-intervention 30 min intervals are matched on irradiance, ambient temperature, relative humidity, and wind speed under hard calipers, with day-clustered confidence intervals and a co-located, independently metered sub-array used as a control. The analysis yielded 376 matched pairs and a mean power increase of 0.518 kW (95% confidence interval, CI: 0.321–0.714 kW; 28.3%), while the control sub-array showed no comparable gain.
- A field demonstration on an operating 26.73 kWp rooftop installation, implemented with a commercial off-the-shelf UAV, existing SCADA metering, and open-source software (OpenDroneMap v3.6.0 and GRASS GIS v8.5.0). The open-circuit fault was traced progressively from the aerial thermogram to a specific protection device in the direct-current (DC) distribution enclosure, its energy impact was estimated at approximately 6088 kWh per year, and a standards-based test sequence is defined for the fault that remained unresolved after the intervention.

The remainder of this paper is organized as follows. Section 2 describes the materials and methods, comprising the study site and experimental setup (Sections 2.1 and 2.2), the UAV thermographic inspection protocol (Section 2.3), the thermal anomaly taxonomy (Section 2.4), the image-processing pipeline (Section 2.5), the electrical performance analysis and root-cause verification procedures (Section 2.6) and the diagnostic algorithm with its decision rules (Section 2.8). Section 3 presents the results of the case study: the monitoring period and weather characterization (Section 3.1), the UAV survey products and detected thermal anomalies (Section 3.2), the maintenance intervention (Section 3.3), the root-cause attribution of the open-circuit fault and of the shading-induced hotspots, together with the weather-matched paired analysis of the SCADA data (Section 3.4), and a summary

of the ground-truth events and diagnostic outcomes (Section 3.5). Section 4 discusses the limitations of the framework and the scope of its applicability. Section 5 draws the conclusions and outlines directions for future work. The parameters of the diagnostic pipeline and of the UAV acquisition are listed in Appendix A.

2. Materials and Methods

2.1. Study Site

The study was conducted on two rooftop photovoltaic installations located on the main campus of the National University of Science and Technology POLITEHNICA Bucharest (UNSTPB), Romania (approximately 44.438° N, 26.051° E). The study site is situated in a temperate-continental climatic region characterized by hot summers, cold winters, and moderate annual solar irradiation, representative of photovoltaic installations operating throughout south-eastern Europe.

The long-term solar resource at the site was obtained from the Photovoltaic Geographical Information System (PVGIS) database developed by the Joint Research Centre (JRC) of the European Commission, providing annual global horizontal irradiation (GHI) and expected photovoltaic energy yield under local climatic conditions. These data were used to characterize the solar resource available at the study location and to place the monitored production within its climatic context.

Two grid-connected rooftop photovoltaic systems installed on university buildings were selected for analysis (Figure 1).

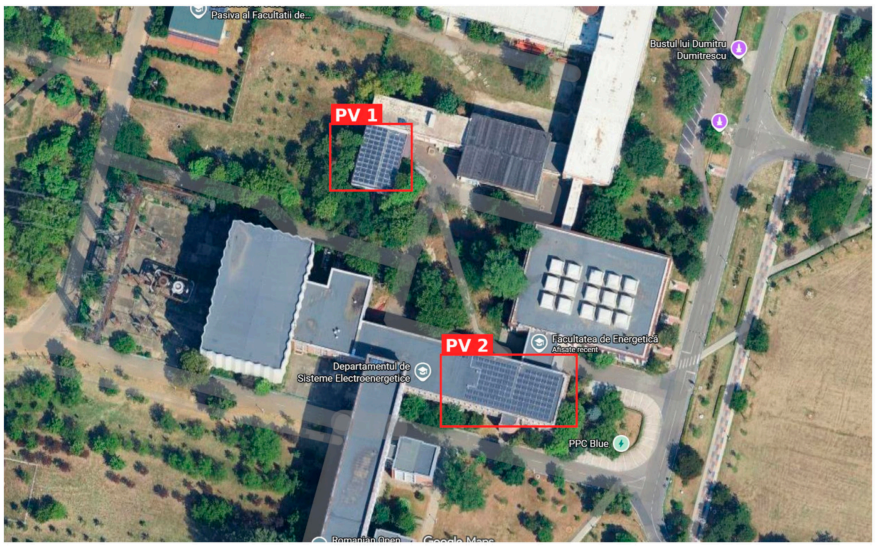


Figure 1. Location of the two rooftop photovoltaic installations on the POLITEHNICA Bucharest campus (satellite view). PV 1 (red box, 26.73 kWp, 81 modules of 330 Wp); PV 2 (red box, 39.27 kWp, 111 modules).

The first installation (PV 1) consists of a 26.73 kWp photovoltaic system composed of 81 monocrystalline silicon modules manufactured by MyLight Systems (Villeurbanne, Lyon, France) rated at 330 Wp each, mounted on a flat rooftop using fixed-tilt galvanized steel support structures inclined at 15°. The system has been operating since 2022 and is continuously monitored through a SCADA platform providing electrical production data used throughout this study.

The second installation (PV 2) consists of a 39.27 kWp photovoltaic system composed of 111 monocrystalline silicon modules of which 69 are rated at 350 Wp, manufactured by Q-Cells, and 42 at 360 Wp, manufactured by Canadian Solar (Kitchener, ON, Canada)

mounted on fixed-tilt support structures inclined at 15°. The system is likewise monitored through a SCADA platform; its production data are not used in the present analysis.

PV 1 is the case-study installation: all quantitative results reported in Section 3, namely thermal anomaly detection, root-cause verification, SCADA analysis, and the pre- and post-intervention comparison, refer to it. PV 2 served as an auxiliary inspection site. It was surveyed with the same flight protocol (Section 2.3) and processed with the same image-processing pipeline (Section 2.5) in order to confirm that the acquisition and processing workflow transfers to an array of different size, layout, and module mix. No electrical validation was carried out for PV 2, because synchronized operational and meteorological measurements were available only for PV 1; PV 2 therefore contributes no ground-truth events or electrical results to this study.

The electrical architecture of both installations follows a conventional hierarchical configuration comprising photovoltaic modules, strings, combiner boxes, maximum power point trackers (MPPTs), and grid-connected inverters. Individual PV modules are connected in series to form strings, while multiple strings are connected in parallel within DC combiner boxes before feeding dedicated MPPT inputs. The MPPT continuously adjusts the operating voltage of each array to maximize power extraction under changing irradiance and temperature conditions, after which the generated DC power is converted into alternating current (AC) by the inverter and supplied to the electrical grid.

2.2. Experimental Setup

The experimental framework combined four complementary sources of information to assess the condition and operational performance of the photovoltaic installations: (i) aerial thermographic inspections acquired using a UAV, (ii) high-resolution RGB imagery for visual assessment, (iii) continuous electrical measurements recorded by the SCADA system, and (iv) on-site meteorological observations. The integration of these datasets enabled thermal anomalies identified during aerial inspections to be correlated with the electrical behaviour of the photovoltaic system under actual operating conditions, while minimizing the influence of transient environmental factors.

The experimental workflow adopted in this study is illustrated in Figure 2.

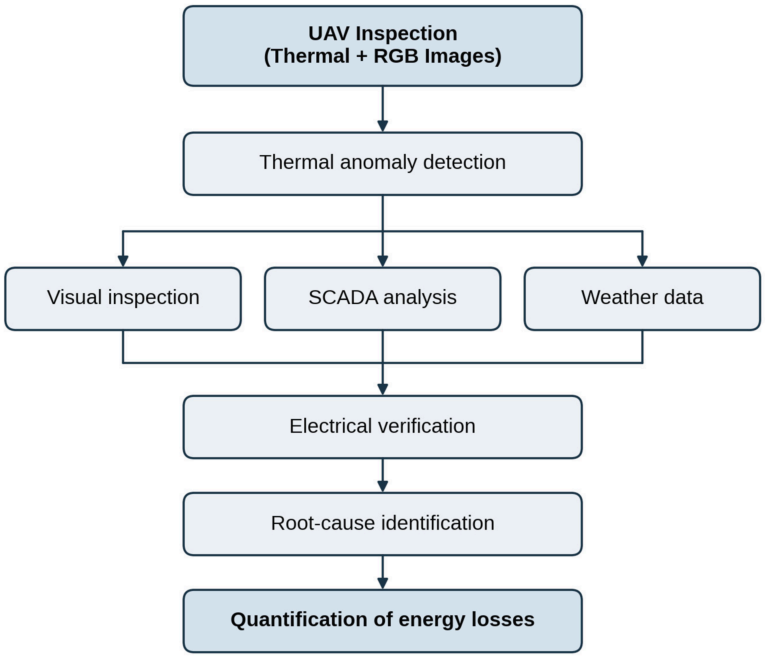


Figure 2. Experimental workflow of the integrated diagnostic framework.

UAV-acquired thermal and RGB imagery were first processed to identify abnormal temperature distributions across the photovoltaic array. The detected anomalies were subsequently verified through visual inspection and correlated with synchronized SCADA measurements and meteorological observations. Finally, targeted electrical measurements and ground-based thermographic inspections were performed to determine the physical origin of each anomaly and evaluate its influence on power production.

The following subsections describe the equipment employed throughout the experimental campaign.

2.2.1. Unmanned Aerial Platform

Aerial inspections were performed using a DJI Mavic 3 Thermal (Mavic 3T) (DJI, Shenzhen, China), a quadcopter specifically designed for industrial inspection applications. The platform integrates a radiometric thermal infrared camera, a high-resolution RGB camera, and a GNSS positioning system within a compact and highly stable aerial platform, making it particularly suitable for photovoltaic inspection.

The thermal imaging payload consists of an uncooled vanadium oxide (VOx) microbolometer with a spatial resolution of 640 × 512 pixels operating within the 8–14 µm long-wave infrared spectral range. Unlike conventional thermal cameras that provide only colourized temperature maps, the radiometric sensor records the absolute temperature associated with every pixel, allowing quantitative thermal analysis to be performed during post-processing [17]. Complementary visual information was acquired using the integrated 48-megapixel RGB camera, enabling the identification of surface contamination, vegetation, physical damage, shadows, and other visible features that could influence the thermal behaviour of photovoltaic modules. The simultaneous acquisition of thermal and RGB imagery facilitated the distinction between intrinsic module defects and reversible environmental phenomena. The UAV incorporates a three-axis stabilized gimbal, ensuring constant camera orientation during flight and minimizing image distortion caused by aircraft motion. Positioning information recorded by the onboard GNSS receiver enabled each thermal image to be accurately georeferenced and subsequently related to the physical location of individual photovoltaic modules within the array.

2.2.2. Meteorological Monitoring

Meteorological monitoring was carried out using a Sainlogic (Shenzhen, China) WS3500 weather station, a compact wireless system consisting of an indoor display console and an integrated "7-in-1" outdoor sensor array combining an anemometer, wind vane, rain collector, thermo-hygrometer, and a combined light/UV sensor in a single solar-powered unit. The station therefore records wind speed, wind direction, precipitation, outdoor air temperature, relative humidity, solar irradiance, and UV radiation. Global irradiance is measured by the integrated light sensor, with the readout unit selectable between lux, foot-candles, and W m^{-2}, the latter being the default and the unit adopted in this study. Although the station employs a photodiode-based light sensor rather than a class-compliant pyranometer, the irradiance measurements were used primarily for flight scheduling and relative normalization of electrical performance, for which this accuracy level is sufficient. The outdoor sensor array was mounted on a pole adjacent to the photovoltaic array, free of shading and at a height representative of module-level conditions, and transmitted its measurements wirelessly to the receiving console. Through the console's Wi-Fi connectivity, all observations were automatically uploaded to an online weather data platform, from which the time-stamped records were retrieved and synchronized with the SCADA measurements.

2.2.3. Electrical Monitoring System

Continuous operational data were obtained from the photovoltaic SCADA system. The monitoring platform recorded the principal electrical operating parameters of the installation, including AC power output, voltage, current, inverter operating status, and energy production throughout the observation period.

Electrical energy metering at the plant level was performed using DIN-rail mounted, Measuring Instruments Directive (MID)-certified three-phase energy meters, namely a Carlo Gavazzi (Steinhausen, Switzerland) EM340 and an Algodue UEM80, both installed for direct connection without external current transformers.

The Carlo Gavazzi EM340 is a three-phase energy meter for direct current measurement up to 65 A, with a nominal voltage range of 208–400 V (line-to-line) and an operating frequency range of 45–65 Hz. The instrument complies with accuracy Class 1 for active energy according to EN 62053-21 and Class B according to EN 50470-3, with a reading accuracy of $\pm 0.5\%$.

The Algodue (Maggiora, Piedmont, Italy) UEM80 is a three-phase, four-wire energy meter rated for direct connection up to 80 A (reference current 5 A, starting current 20 mA), operating at $3 \times 230/400$ V to $3 \times 240/415$ V and 50/60 Hz.

Unlike aerial thermography, which provides high spatial resolution but only represents the condition of the installation at the instant of inspection, the SCADA system continuously characterizes the electrical behaviour of the photovoltaic plant. The combination of these complementary datasets therefore allows localized thermal anomalies to be linked directly to variations in electrical performance and long-term energy production.

For the installation selected for detailed analysis, SCADA measurements were available continuously before and after the maintenance intervention, enabling the electrical consequences of the detected defects to be quantified and the effectiveness of the corrective actions to be objectively evaluated.

2.3. UAV Thermographic Inspection Protocol

Thermographic inspections were carried out in accordance with the recommendations of the International Electrotechnical Commission (IEC) in IEC TS 62446-3:2017 [19], the international technical specification governing outdoor infrared inspection of operating photovoltaic systems. The standard establishes the minimum environmental requirements, equipment characteristics, acquisition procedures, reporting methodology, and interpretation criteria necessary to ensure repeatable and reliable thermographic measurements. Compliance with these recommendations minimizes the influence of external factors on the measured thermal signatures and enables meaningful comparison between inspection campaigns.

To evaluate the influence of maintenance interventions on photovoltaic performance, two independent UAV inspection campaigns were conducted. The first survey was performed approximately one month before the corrective intervention to establish the initial thermal condition of the installation, while the second campaign was carried out approximately one month after maintenance activities had been completed. This experimental design enabled a direct comparison of the thermal behaviour of individual photovoltaic modules before and after intervention.

Flight dates were selected based on both weather forecasts and real-time meteorological observations to satisfy the environmental conditions specified by IEC TS 62446-3. Inspections were performed only under stable clear-sky conditions, with in-plane solar irradiance exceeding 600 W m^{-2}, wind speeds below 20 km h^{-1}, and negligible cloud cover. These conditions maximize the thermal contrast between healthy and defective modules while minimizing transient temperature variations caused by changing irradiance or atmospheric conditions [14,20].

All flights were conducted within a time window centred on solar noon, when solar irradiance and photovoltaic operating temperatures reach their daily maximum and thermal anomalies become most distinguishable. The UAV maintained a nadir viewing geometry throughout the inspections. Flight altitude, image overlap, and aircraft velocity were kept constant during all acquisition missions in order to ensure comparable spatial resolution and image quality between surveys [15,17]. All missions were flown at a route altitude of 22.7 m and a speed of 1.3 m s^{-1}, with 75% forward and 85% side image overlap, giving a thermal ground sampling distance of 3.0 cm px^{-1}, consistent with the geometric resolution recommended by IEC TS 62446-3; the complete set of acquisition and thermal camera parameters is listed in Table A2 (Appendix A).

Prior to each inspection campaign, the thermal camera parameters were configured according to the environmental conditions prevailing at the site. Surface emissivity, reflected apparent temperature, and atmospheric parameters were adjusted following the manufacturer's recommendations and the guidance provided by IEC TS 62446-3. Emissivity was set to 0.95 for the glass-covered monocrystalline modules. Because the diagnostic rules of Algorithm 1 rest on temperature differences between modules imaged under identical settings, a moderate deviation of the true emissivity from this value would shift the absolute temperatures without changing the classification of the anomalies reported here. All radiometric thermal images were stored in their original format, preserving the absolute temperature information associated with every pixel for subsequent quantitative analysis.

Table 1. Principal characteristics of the thermal abnormalities considered in this study, compiled from [11,14,19,20].

Thermal Anomaly	Typical Thermal Signature	Primary Causes	Reversible	Typical Corrective Action
Hotspot	Localized high-temperature region affecting one or several cells	Cell defects, microcracks, contamination, partial shading	Sometimes	Cleaning, removal of shading, module replacement if permanent
Bypassed substring	Uniform heating over approximately one-third or two-thirds of the module	Temporary shading, soiling, bird droppings, defective bypass diode	Usually	Remove shading or contamination; replace module if persistent
Potential-Induced Degradation (PID)	Elevated temperatures concentrated along module edges	Leakage currents caused by high system voltage	Generally No	Grounding optimization, anti-PID device, module replacement if severe
Open-circuit fault	Uniform overheating of all modules belonging to one electrical string	Blown fuse, disconnected cable, defective connector or breaker	Yes	Repair or replace the faulty electrical component

The acquired thermal dataset was complemented by synchronized high-resolution RGB imagery obtained during the same flight missions. While thermal images were used to identify abnormal temperature distributions indicative of electrical faults, the RGB photographs provided additional information regarding module contamination, vegetation, structural shading, physical damage, and other visible factors capable of influencing the thermal response of the photovoltaic array. The combined interpretation of thermal and visual imagery reduced the possibility of misclassifying reversible environmental effects as intrinsic module defects [22].

Algorithm 1. Diagnostic pipeline (Parameter values are listed in Table A1)

Inputs: radiometric thermal frames and RGB images with GNSS metadata; string layout of the array; SCADA records for each independently metered region; weather-station records.
Output: for each anomaly, its location, fault class, cause, severity, recommended action, and verification status.

1. Acquisition gate. Accept a flight only if the in-plane irradiance is at least $G_{\min}$, the wind speed is below $v_{\max}$, the sky is clear, and the view is nadir (IEC TS 62446-3).
2. Survey products. Reconstruct the RGB orthomosaic, the dense point cloud, and the DSM (resolution r_{DSM}) with OpenDroneMap. Keep the original radiometric frames for all temperature measurements; use the thermal orthomosaic for visualization only.
3. Candidate selection (Level 1).
   - 3a. Segment the modules in each radiometric frame. Compute the median temperature T_{m} of every module and the frame reference T_{f} as the median over all segmented modules.
   - 3b. Detector path: retain detector outputs with confidence of at least τ_{c} and discard those that fail the glare criterion.
   - 3c. Radiometric path, applied to every module irrespective of 3b: flag module m if $T_{\mathrm{m}} - T_{\mathrm{f}} \geq \Delta T_{\mathrm{mod}}$; flag a cell-level candidate if the maximum pixel temperature in the module exceeds T_{m} by at least ΔT_{cell}.
   - 3d. Take the union of 3b and 3c as the candidate set and assign each candidate to a module and a string through the georeferenced layout.
4. Class hypothesis (Level 2). Assign the class from the spatial pattern (Table 1): cell-level exceedance → hotspot; one-third or two-thirds of a module → bypassed substring; edge or corner heating repeated along a string → PID; all modules of one string flagged in 3c with a uniform elevation → open-circuit fault.
5. Shading quantification. For the timestamp of each frame that contains a candidate, run r.sun on the DSM and set the shadow mask where the direct-beam irradiance is zero. For each candidate module compute the shaded fraction f_{s}, the share of the module footprint. Label the candidate shading-confirmed if $f_{\mathrm{s}} > 0$ and the co-registered RGB frame shows a cast shadow or an obstruction on the same module, shading-possible if only one of the two conditions holds, and unshaded otherwise. Repeat r.sun over the diurnal cycle to obtain the hours in which the module is shaded.
6. SCADA test of the hypothesis. For the metered region that contains the candidate, compute the output normalized to installed capacity in 30 min bins with irradiance of at least G_{match}, and its deficit D_{obs} relative to the expected output, taken from a co-located reference region or from the region's own power–irradiance relation in a fault-free period. Compute the deficit D_{exp} implied by the hypothesis: for an open-circuit fault, the share of the region's capacity in the affected string, present in all bins; for shading, a deficit confined to the hours found in Step 5. The hypothesis is supported if $|D_{\mathrm{obs}} - D_{\mathrm{exp}}| \leq \delta$, not testable if $D_{\mathrm{exp}} < \delta$, and contradicted otherwise.
7. Contradictory evidence. Evidence is ranked in the order field electrical measurement, SCADA, radiometric rule and shading model, detector.
   - 7a. A shading-confirmed or shading-possible candidate whose SCADA deficit is not confined to the predicted shading hours, or which persists in a frame acquired; reject the shading hypothesis, reclassify as a possible intrinsic fault, and go to Step 8.
   - 7b. An unshaded candidate with a contradicted SCADA test (the expected deficit is absent): re-examine the overlapping frames for reflection or emissivity artefacts; if the signature persists, go to Step 8.
   - 7c. A SCADA deficit with no thermal candidate in the region: schedule a targeted re-survey and string-level measurements at the combiner box.
   - 7d. Detector path and radiometric path disagree: keep the candidate, since recall is favoured, and let Steps 5 and 6 decide.
   - 7e. A candidate that is not testable in Step 6: keep it, record its ΔT, and re-survey it at the next campaign. No corrective action other than field verification is taken while a contradiction is unresolved.
8. Field verification (closes Level 2). Visual inspection; open-circuit voltage and current of the suspect string at the combiner box compared with the parallel strings; continuity, connector, and fuse checks; handheld thermography along the DC path. The field result overrides Steps 4–7.
9. Severity (Level 3). Record ΔT against the healthy reference and estimate the energy loss of the affected capacity with PVWatts.
10. Action and verification (Level 4). Select the corrective action from the confirmed cause. After the intervention, match each pre-intervention bin to its nearest post-intervention bin in the standardized space of irradiance, ambient temperature, relative humidity, and wind speed under the calipers of Table A1, discard unmatched bins, and compute the mean paired difference with a day-clustered 95% confidence interval for the treated region and for a control region. The intervention is verified if the interval of the treated region excludes zero and the control region shows no change in the same sign.

2.4. Thermal Anomaly Taxonomy

The interpretation of aerial infrared images was based on the thermal abnormality classes defined in IEC TS 62446-3, which provides standardized guidance for the diagnosis of photovoltaic faults using infrared thermography. Although numerous degradation mechanisms may occur throughout the lifetime of a photovoltaic module [7], only a limited number produce characteristic thermal signatures that can be reliably identified during aerial inspection [11,14,20]. The framework screens for four principal anomaly classes: hotspots, bypassed substrings, PID, and open-circuit faults. Of these, hotspots and open-circuit faults were observed on the studied arrays, whereas bypassed substrings and PID were not (Section 3.4.4). Sections 2.4.2 and 2.4.3 therefore describe reference signatures used for screening and are not findings of this study. Representative thermal patterns corresponding to each anomaly are presented in Figures 3–6.

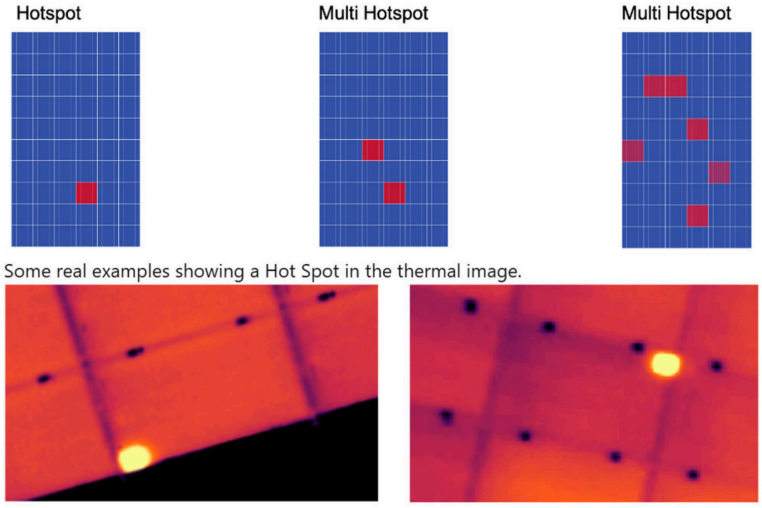


Figure 3. Infrared thermographic images of modules in the field exhibiting a hotspot. The false-color scale maps surface temperature from coolest (dark purple/black) to hottest (yellow/white); the uniform orange area corresponds to the normal operating temperature of the module.

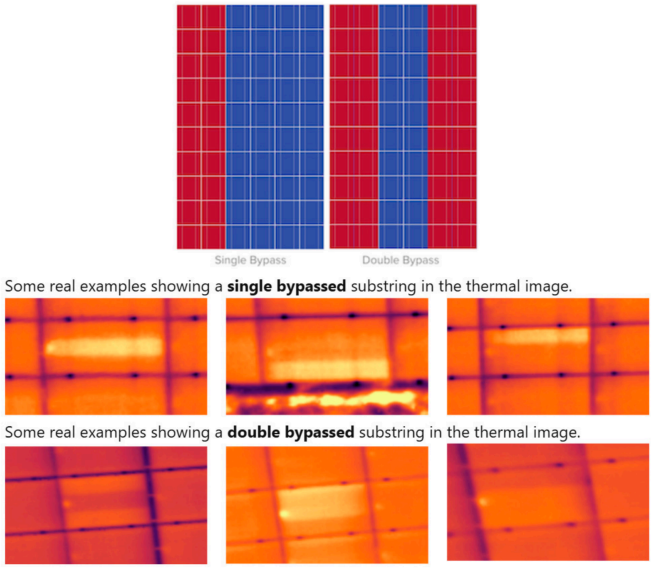


Figure 4. Representative thermal patterns associated with bypassed substrings. The false-color scale maps surface temperature from coolest (dark purple/black) to hottest (yellow/white); the uniform orange area corresponds to the normal operating temperature of the module. Source: Sitemark.

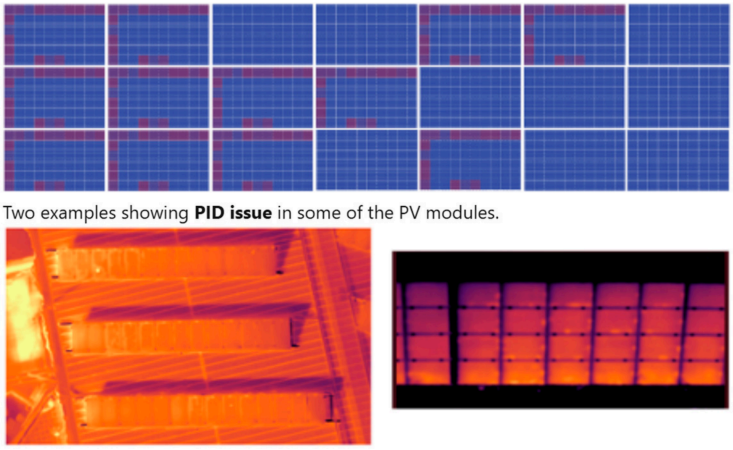


Figure 5. Representative thermal patterns associated with potential-induced degradation (PID). The false-color scale maps surface temperature from coolest (dark purple/black) to hottest (yellow/white); the uniform orange area corresponds to the normal operating temperature of the module. Source: Sitemark.

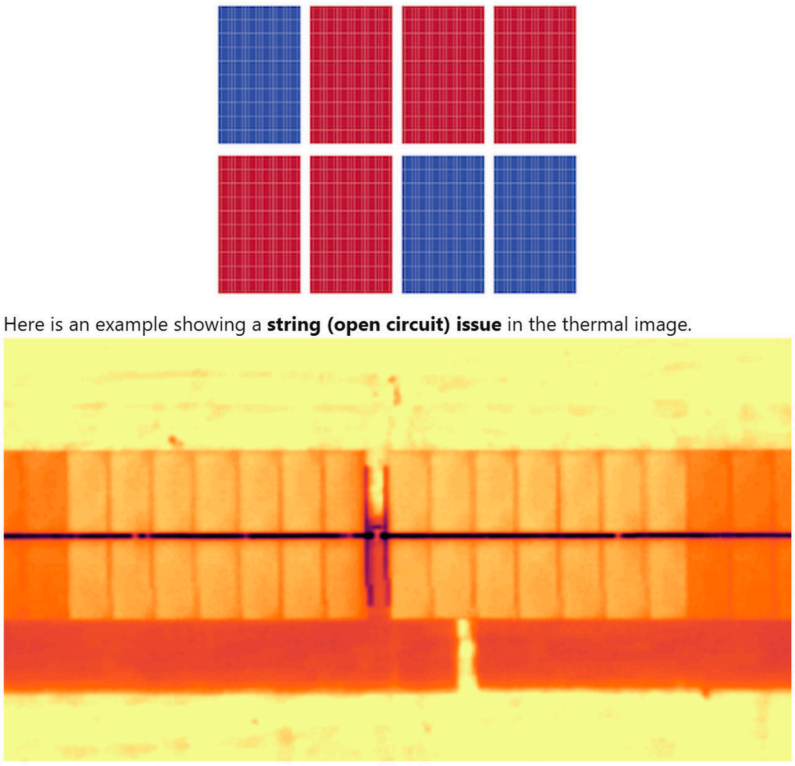


Figure 6. Representative thermal patterns associated with open-circuit faults. The false-color scale maps surface temperature from coolest (dark purple/black) to hottest (yellow/white); the uniform orange area corresponds to the normal operating temperature of the module. Source: Sitemark.

2.4.1. Hotspots

Hotspots represent the most frequently encountered thermal anomaly in photovoltaic installations. They occur when one or more photovoltaic cells dissipate electrical power as heat instead of converting solar irradiance into electricity. This localized temperature increase may originate from intrinsic cell defects, microcracks, manufacturing imperfections, localized shading, contamination, vegetation, bird droppings, or electrical degradation of the module [11,14,37].

During thermographic inspection, hotspots appear as localized regions exhibiting significantly higher temperatures than neighboring cells or adjacent modules (Figure 3).

The magnitude of the temperature difference generally depends on the severity of the underlying defect and the prevailing irradiance conditions. Because prolonged hotspot operation accelerates module degradation and may eventually lead to permanent damage, their early identification is essential for preventive maintenance.

2.4.2. Bypassed Substrings

Modern crystalline silicon photovoltaic modules are internally divided into multiple series-connected substrings protected by bypass diodes. Under normal operating conditions, these diodes remain reverse biased and do not conduct. However, when one substring becomes shaded or electrically damaged, the corresponding bypass diode conducts, allowing current to flow around the affected cells and preventing excessive power dissipation.

Thermographically, bypass diode activation appears as a uniformly heated region covering approximately one-third or two-thirds of the module surface, corresponding to the affected substring (Figure 4) [11,14]. This thermal pattern is frequently associated with temporary shading caused by vegetation, accumulated dirt, bird droppings, or nearby structures, although persistent activation may also indicate permanent electrical defects within the module.

Because many bypass-substring anomalies originate from reversible external causes, visual inspection should always accompany thermographic analysis before maintenance decisions are made.

2.4.3. Potential-Induced Degradation (PID)

PID is one of the most significant electrically induced degradation mechanisms affecting crystalline silicon photovoltaic modules operating under high-voltage conditions. The phenomenon results from the electrical potential difference established between the photovoltaic cells and the grounded module frame, which promotes leakage currents through the encapsulation materials. Over prolonged periods of operation, these leakage currents facilitate the migration of sodium ions from the front glass into the anti-reflective coating and the p–n junction of the solar cells, increasing carrier recombination and reducing module output power [7,11].

Unlike temporary thermal anomalies caused by shading or contamination, PID generally develops progressively over months or years and may affect multiple modules connected within the same string. Consequently, the degradation frequently exhibits a characteristic spatial distribution rather than appearing as an isolated module defect.

During infrared inspection, PID is typically identified by elevated temperatures concentrated near one edge or one corner of the module, producing irregular edge-heating patterns (Figure 5) [11,35]. In severe cases, neighbouring modules located at the same electrical potential within the string may exhibit similar thermal signatures, allowing the degradation to be recognized at the array level.

Although several mitigation strategies have been proposed, including improved system grounding, modification of inverter operating modes, installation of anti-PID recovery devices, or rearrangement of module positions within the string, complete recovery is not always possible once permanent cell degradation has occurred. Consequently, early detection remains essential for limiting long-term performance losses.

2.4.4. Open-Circuit Faults

Open-circuit faults constitute severe electrical abnormalities encountered in photovoltaic systems because they interrupt current flow through an entire string or circuit section. These faults are typically caused by disconnected cables, blown fuses, damaged connectors, broken conductors, defective circuit breakers, or failed electrical joints within the DC circuit.

Under normal operating conditions, photovoltaic modules convert a significant proportion of the absorbed solar irradiance into electrical energy. When current flow is interrupted, this energy conversion process ceases and the absorbed solar radiation is dissipated almost entirely as heat. As a result, the affected modules exhibit temperatures considerably higher than neighbouring strings operating under identical irradiance conditions.

Thermographically, open-circuit faults are characterized by a nearly uniform temperature increase affecting every module belonging to the disconnected string (Figure 6) [11,36]. Because the thermal signature extends across multiple consecutive modules following the electrical topology of the installation, this type of anomaly can usually be distinguished from localized degradation mechanisms such as hotspots or PID.

From an operational perspective, open-circuit faults are associated with substantial power losses because the affected string contributes little or no electrical energy to the overall system output. Nevertheless, they are frequently among the easiest defects to repair once their location has been identified, as corrective actions generally involve replacing defective protection devices, reconnecting electrical conductors, or repairing damaged cable terminations. For this reason, early identification of open-circuit faults is particularly important for minimizing energy losses.

2.4.5. Summary of Thermal Abnormalities

The thermal anomalies considered in this study differ substantially with respect to their physical origin, characteristic thermal signature, impact on electrical performance, and maintenance requirements. While some abnormalities originate from temporary environmental factors, such as vegetation, soiling, or partial shading, others are caused by irreversible degradation processes occurring within the photovoltaic module or electrical system. Consequently, the interpretation of thermal images should never rely solely on temperature distribution but should be supported by complementary information obtained from RGB imagery, electrical measurements, and operational data. The principal characteristics of the four anomaly classes are summarized in Table 1.

2.5. Image Processing Pipeline

The processing of the aerial datasets followed a multi-stage workflow designed to preserve the radiometric integrity of the thermal imagery while enabling the spatial analysis of photovoltaic modules and the identification of environmental factors influencing their thermal response. The complete image-processing workflow is summarized in Figure 7.

The raw thermal infrared and RGB images acquired during each UAV flight were initially processed independently. High-resolution RGB photographs were used to generate georeferenced orthomosaics and three-dimensional surface models, while the radiometric thermal images were retained in their original format for quantitative temperature analysis.

Orthomosaic generation was performed using OpenDroneMap (ODM), an open-source photogrammetric software package implementing Structure-from-Motion (SfM) and Multi-View Stereo (MVS) reconstruction algorithms. The software automatically aligned overlapping images, estimated camera positions, reconstructed a dense point cloud, and generated georeferenced orthomosaics [22,36].

Although thermal orthomosaics provide an intuitive visualization of the entire photovoltaic installation, they were not used for quantitative temperature measurements. During the mosaicking process, overlapping images undergo geometric correction, interpolation, resampling, and radiometric blending, operations that inevitably modify the original pixel temperatures. Since the objective of this study was to analyse temperature differences at the module level, all quantitative thermal analyses were performed directly on the original radiometric images exported from the UAV, as in frame-based processing pipelines [35,36].

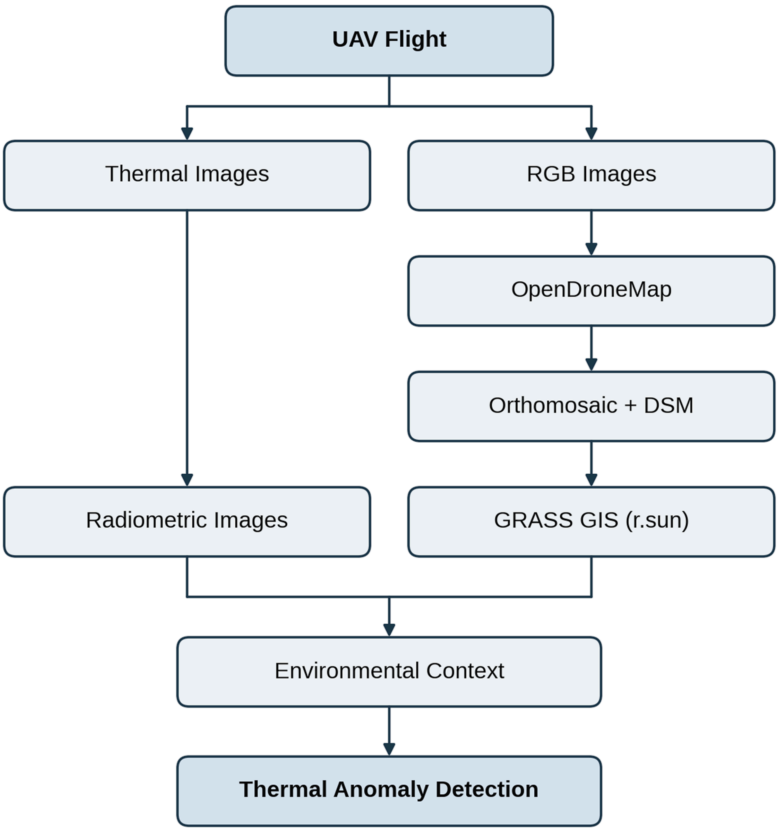


Figure 7. Workflow for UAV-based thermal anomaly detection in PV modules. Thermal images are converted to radiometric images; RGB images are processed in OpenDroneMap to produce an orthomosaic and DSM, used to compute solar irradiance in GRASS GIS (r.sun). Both streams provide environmental context for anomaly detection. Arrows indicate data flow; dark boxes mark workflow input and output, light boxes intermediate steps.

In contrast, the RGB orthomosaic and the dense point cloud generated by ODM constituted valuable ancillary datasets. The dense point cloud was used to derive a DSM representing the geometry of buildings, photovoltaic arrays, and surrounding obstacles. This DSM was subsequently imported into GRASS GIS, where the r.sun solar radiation model was employed to estimate the spatial distribution of solar irradiance across the rooftop and identify surfaces potentially responsible for partial shading of the photovoltaic modules.

Implementing physical models as raster workflows in open-source GIS has proved practical for site-scale environmental assessment, including a recent pollutant-dispersion application on the same university campus [42]; the r.sun shading analysis used follows a similar approach.

The integration of thermal imagery, RGB orthomosaics, and DSM-derived shading maps enabled each detected thermal anomaly to be interpreted within its environmental context. This approach reduced the likelihood of falsely classifying temporary shading or vegetation effects as intrinsic photovoltaic defects and provided additional evidence during the root-cause attribution process.

The outputs generated by the image-processing pipeline consisted of georeferenced RGB orthomosaics, thermal orthomosaics for visualization purposes, radiometric thermal images for quantitative analysis, dense point clouds, DSMs, and solar irradiance and shading maps derived from the DSMs.

These products formed the spatial information layer used throughout the subsequent anomaly detection and root-cause analysis.

2.6. Electrical Performance Analysis

While UAV thermography provides detailed spatial information regarding the thermal condition of individual photovoltaic modules, it represents only the instantaneous state of the installation at the time of inspection. To evaluate the operational significance of the detected anomalies, thermal observations were complemented by continuous electrical measurements acquired through the SCADA system.

The SCADA platform continuously recorded the principal operating parameters of the photovoltaic installation, including AC power output, inverter operating status, and cumulative energy production. These measurements provided a continuous description of system performance throughout the monitoring period and enabled the electrical consequences of the identified thermal anomalies to be quantified.

Electrical data were synchronized with the corresponding UAV inspection campaigns using their acquisition timestamps. For each inspection, electrical measurements recorded under comparable irradiance and environmental conditions were extracted to ensure that observed performance variations were primarily associated with module degradation rather than short-term meteorological fluctuations.

Because photovoltaic power production is strongly dependent on environmental conditions, the electrical analysis incorporated the meteorological observations presented in Section 2.2. Variations in solar irradiance, ambient temperature, and wind speed were considered during the interpretation of production data to reduce the influence of climatic variability on the comparison between inspection campaigns [32].

The effectiveness of the corrective maintenance was assessed by comparing the electrical performance of the installation before and after the intervention. Changes in power production, energy yield, and operational stability were evaluated together with the corresponding thermographic observations, allowing improvements in electrical performance to be directly associated with the elimination of the detected faults.

Rather than considering thermographic and electrical datasets independently, the proposed methodology integrates both sources of information to establish a direct relationship between localized thermal abnormalities and their impact on overall system performance. This combined analysis provides a more reliable assessment of fault severity than either technique used in isolation [20,39].

2.7. Definition of Anomaly Diagnosis and Evaluation Criteria

The identification of a thermal anomaly does not necessarily reveal the physical mechanism responsible for its occurrence. Similar temperature distributions may originate from different electrical faults or environmental conditions, making additional verification essential before maintenance decisions are undertaken [14,20]. For this reason, all anomalies detected during the UAV inspections were subjected to a systematic root-cause analysis combining thermal observations, visual inspection, electrical measurements, and field verification.

The term anomaly diagnosis is applied in the literature to tasks ranging from the flagging of a thermal abnormality to the recommendation of a maintenance action [12,24,25,30]. In this study it denotes a sequence of four levels, each of which takes the result of the preceding level as its input and is evaluated with its own metric:

- Level 1, detection and localization: establishing that a thermal abnormality is present and assigning it to a physical element of the installation (cell, module, or string) in the georeferenced survey products. This level is evaluated by the agreement between the automated detections and a reference set established by manual interpretation of the aerial imagery and by ground inspection, expressed as the number of reference anomalies detected, the number missed, and the number of detections not confirmed.

- Level 2, fault-type identification and root-cause attribution: assigning each localized abnormality to one of the classes of Section 2.4 and to its physical origin, and in particular separating intrinsic electrical faults from reversible environmental effects such as shading or soiling. This level is evaluated by confirmation of the image-based classification through independent evidence, namely the radiometric comparison with neighbouring healthy strings, the r.sun cast-shadow simulation and RGB imagery, string-level electrical measurements, and ground-based thermography (Section 2.8).
- Level 3, severity quantification: expressing the consequence of a confirmed anomaly in thermal terms, as the temperature difference ΔT relative to a healthy reference operating under the same irradiance, and in electrical terms, as the power or energy loss attributable to it. The metrics are ΔT (K) and the estimated energy loss (kWh per year).
- Level 4, maintenance decision support: selecting the corrective action that follows from Levels 1–3 and verifying its effect once it has been carried out. The framework supplies evidence to the operator and does not automate the decision. This level is evaluated by the weather-matched change in power output after the intervention, reported with its 95% confidence interval and compared with a co-located control sub-array (Section 3.4.3).

Prognosis, understood as the prediction of future degradation rates or of remaining useful life, lies outside the scope of the framework; severity is therefore reported only for the condition observed at the time of inspection. Because the four levels differ in kind, no single aggregate performance figure is reported. In particular, statistical detection metrics such as precision and recall cannot be estimated reliably from a single 81-module installation and are not claimed; the Level 1 results describe agreement on the investigated installation only. The quantitative assessment of detection accuracy, fault-type identification accuracy, false-positive reduction, and baseline strategies is left to future work (Section 5). The outcomes obtained at each level are summarized in Section 3.5.

2.8. Diagnostic Algorithm and Decision Rules

Algorithm 1 states the diagnostic pipeline of Sections 2.3–2.7 as an explicit sequence of steps and decision rules. Figures 2 and 7 give the corresponding workflow diagrams, and Table A1 (Appendix A) lists the parameter values needed to reproduce it. The algorithm specifies how thermographic candidates are selected (Step 3), how shading is quantified from the DSM and the RGB imagery (Step 5), how SCADA evidence is used to accept or reject a fault hypothesis (Step 6), and how contradictory evidence is handled (Step 7).

Rules 7a–7e were not triggered in the case study, in which the thermal, shading, and field evidence pointed to the same cause for both anomaly types. The one conflict arose in the field (Step 8): the tripping of the protective device on reconnection of the open-circuited string contradicted the initial hypothesis of a simple open contact. In line with the ranking of Step 7, the electrical observation prevailed and the fault was referred to the test sequence described in Section 3.4.1.

3. Results

3.1. Monitoring Period and Weather Characterization

The PV 1 array is divided into two distinct monitoring regions, designated MAC03 and MAC04, the identifiers under which the two independently metered sub-arrays are registered in the plant's SCADA system, as illustrated in the aerial view of the site in Figure 8. The two regions differ in size: MAC03 comprises 18 photovoltaic modules rated at 330 Wp each, corresponding to an installed capacity of 5.94 kWp, while MAC04 comprises the remaining 63 modules of the same 330 Wp type, corresponding to 20.79 kWp, for a total plant capacity of 26.73 kWp distributed over 81 modules. Each monitoring region is equipped with its

own dedicated metering infrastructure and is integrated into the plant's SCADA system, enabling the independent acquisition of electrical and operational parameters at the regional level. This segmentation of the measurement architecture ensures that the energy production, performance indicators, and potential anomalies of each region can be recorded and evaluated separately, without aggregation-induced loss of detail. Consequently, the analysis presented in this work is carried out on a per-region basis, allowing for a direct comparison between MAC03 and MAC04 and for the identification of localized performance deviations that would otherwise remain concealed in plant-level measurements.



Figure 8. Aerial view of the PV 1 rooftop array showing the two independently metered SCADA monitoring regions used in the electrical analysis: MAC03 (red outline; 18 modules, 5.94 kWp) and MAC04 (green outline; 63 modules, 20.79 kWp).

The joint electrical–meteorological dataset covered the period 29 March–18 June 2026 (82 calendar days), of which 77 were producing days with a valid logger day-file. Five days were lost to Raspberry Pi logger outages: no day-file was recorded on 2–3 April and 24 April, and a 71 h interruption spanning 4–7 April removed 5–6 April entirely and left only partial records for 4 and 7 April. A separate weather-station communication gap affected 21–24 April. Raw logger availability was therefore 77 of 82 days (93.9%). After application of the plausibility gates and the minimum-sample requirement, 3543 valid 30 min bins were retained (90.0% of the 3936 nominal bins in the 82-day period), of which 1999 belonged to the daytime subset defined by the irradiance floor of 20 W m^{-2}.

Meteorological conditions during the campaign were characteristic of the late-spring transition in southern Romania. Because the weather station logged independently of the Raspberry Pi, meteorological statistics are reported over the full 82-day period, excluding only the 21–24 April communication gap. Daily global horizontal insolation ranged from

0.68 kWh m^{-2} (2 April, overcast with precipitation) to 7.25 kWh m^{-2} (13 June), with a period mean of 5.0 kWh m^{-2}. Ambient temperature varied between 2.4 °C and 33.2 °C and relative humidity between 20% and 96%, while wind conditions at the sheltered rooftop site were consistently calm, remaining below 3 m s^{-1} for 98% of daytime bins and never exceeding 5 m s^{-1}. Measurable rainfall was recorded on 25 days, with maximum daily accumulations of 45.5 mm (22 May) and 40.1 mm (12 June).

On the basis of the clearness index and the intra-day variability metric, each producing day was assigned to one of four phenomenological day types. Three producing days (21–23 April) could not be classified because the weather-station gap left no irradiance record from which to compute the clearness index, so the classification covers 74 of the 77 producing days: 40 clear days (54.1%), 24 variable days (32.4%), 4 overcast days (5.4%) and 6 rainy days (8.1%), with percentages referring to the 74 classified days. Rainy days are those on which precipitation coincided with a suppressed clearness index throughout daylight hours; the 25 days with measurable rainfall include many on which a brief shower fell on an otherwise clear or variable day, and these retain their radiative classification.

Representative daily production profiles for each day type are shown in Figure 9, illustrating the smooth quasi-sinusoidal profile of clear days, the high-frequency fluctuations characteristic of variable conditions, and the strongly attenuated output under overcast skies.

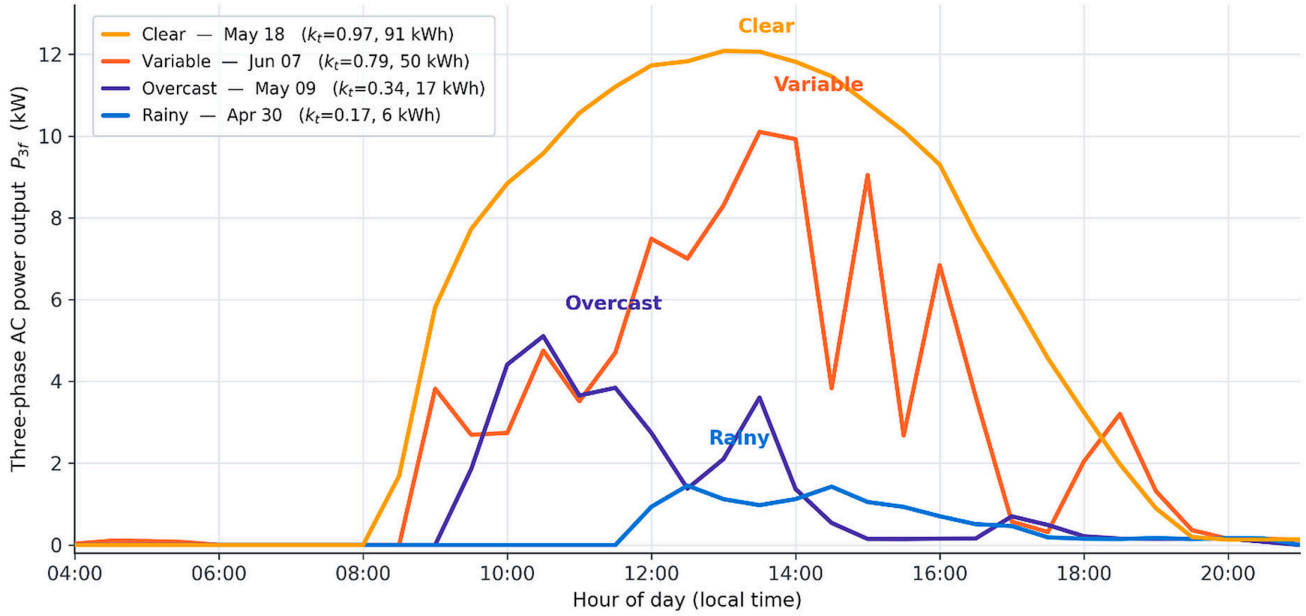


Figure 9. Representative daily AC power profiles of the MAC04 region for each of the four day types identified from the clearness index kt and the intra-day variability metric.

Independently of the rule-based typology, unsupervised k-means clustering applied to the standardized bin-level meteorological variables (irradiance, temperature, relative humidity, and wind speed) identified six empirical weather regimes, selected near the maximum silhouette score of ≈0.28 over the candidate range 4–8. The silhouette curve was essentially flat across k = 5–6 (0.276 at k = 5 and 0.275 at k = 6, versus 0.269 at k = 4 and $\leq$0.26 for k $\geq$ 7), so six regimes were retained for interpretability. The resulting regimes split into three low-irradiance groups—still/damp overcast, warm hazy low-sun, and cool breezy overcast—and three bright clear-sky groups—bright-and-cool, bright warm-and-breezy, and hot bright peak-sun—whose composition is summarized in Table 2.

Table 2. Empirical weather regimes identified by k-means clustering: number of bins, mean irradiance, ambient temperature, relative humidity (RH),and wind speed.

Regime	Bins	Share	Irradiance (W m^{-2})	Temp (°C)	RH (%)	Wind (m s^{-1})
R1—Overcast, cool & humid	453	22.70%	143	14.2	79	0.4
R2—Dull, warm & dry	355	17.80%	184	23.6	49	0.8
R3—Overcast, cool & breezy	158	7.90%	200	14.1	74	1.8
R4—Broken-cloud/hazy, cool	321	16.10%	481	15.3	46	0.9
R5—Bright & clear, warm & windy	218	10.90%	538	22.5	46	2.4
R6—Clear, hot	494	24.70%	655	25.7	46	0.9
All daytime	1999	100%	398	20.4	55	1

3.2. UAV Survey Products and Thermal Anomaly Detection

The output of the automated defect-detection pipeline is presented in Figure 10, which shows the radiometric thermal orthomosaic of the installation, generated by photogrammetric mosaicking of the individual aerial thermograms, together with the resulting defect annotations: the regions delineated in red correspond to detected hotspots, while the region delineated in green corresponds to the open-circuited string. The detections were produced by an ensemble of experimental deep-learning models based on the YOLO architecture, combined with glare filtering and DSM-based shading analysis. Following detection, the candidate segmentation masks are subjected to a radiometric verification stage in which their mean surface temperature is compared against that of neighbouring, electrically healthy arrays: a uniform string-level temperature elevation relative to the adjacent strings confirms the open-circuit classification, whereas localized cell-level exceedances are attributed to hotspots. The hotspots themselves are identified by a YOLO-derived model trained specifically on hotspot signatures and other module-level defect classes. The convergence of the model predictions and the comparative radiometric analysis yielded a largely automated diagnosis that was consistent with the manual aerial and ground-based findings reported in t sections below. On the investigated installation, the automated pipeline identified the open-circuited string, subsequently confirmed by electrical continuity testing, and 14 hotspot regions, of which 14 coincided with the shading-induced hotspots verified by ground thermography (Section 3.4); no anomaly identified through manual aerial or ground inspection was absent from the automated output. Of the four anomaly classes considered (Section 2.4), only these two occurred on the installation, so that the ground truth comprises 15 events arising from two physical causes (Section 3.5). These figures describe agreement on a single 81-module installation under the acquisition conditions of this campaign and are not intended as generalizable performance metrics; the quantitative evaluation of the detection models, including precision, recall and cross-site generalization, is the subject of a separate dedicated study.

The module-level segmentation and radiometric verification stages of the pipeline are illustrated in Figure 11. Subfigure (a) presents the output of the mask-detection stage, in which the segmentation model delineated all twenty-four photovoltaic modules within the aerial thermogram, each detection being assigned a confidence score of 100. Subfigure (b) presents the subsequent thermal analysis performed on these masks, in which the median surface temperature of each module was computed from the calibrated radiometric data and compared against the reference median of the frame (49.0 °C). The analysis reveals a distinctly bimodal temperature distribution: the modules highlighted in blue operate at approximately 44–46 °C, corresponding to normally functioning strings in which the absorbed irradiance is partially converted into electrical energy, whereas the modules highlighted in red exhibit uniformly elevated median temperatures of approximately 52–54 °C, with positive deviations of up to +5.3 K from the frame median. This uniform, string-wide temperature elevation, affecting all modules of the string equally rather than isolated cells, is the characteristic

radiometric signature of the open-circuit defect, in which the entire incident irradiance is dissipated thermally due to the absence of current extraction. The mask-based median comparison thereby provides a quantitative, automated confirmation of the open-circuit classification, complementing the object-detection stage and distinguishing the defect from localized cell-level anomalies such as hotspots.

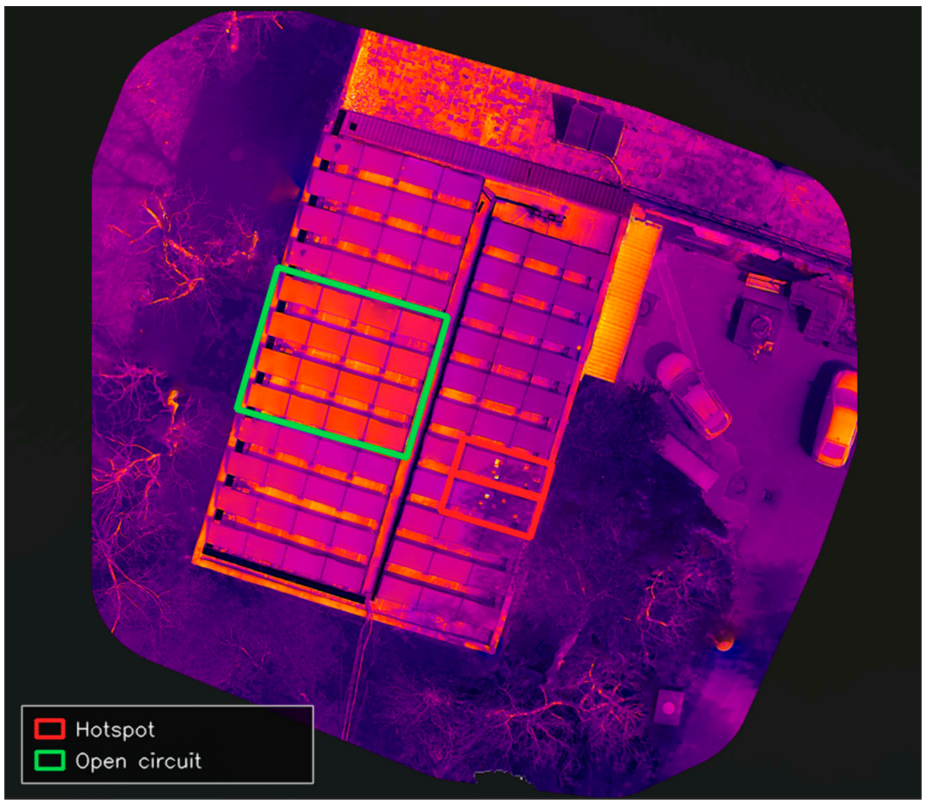


Figure 10. Radiometric thermal orthomosaic of the PV 1 installation, generated by photogrammetric mosaicking of the aerial thermograms, with the output of the automated defect-detection pipeline overlaid: the green box delineates the open-circuited string and the red boxes delineate the hotspot regions detected along the array edge adjacent to the vegetation. The false-color scale maps surface temperature from coolest (dark purple/black) to hottest (yellow/white).

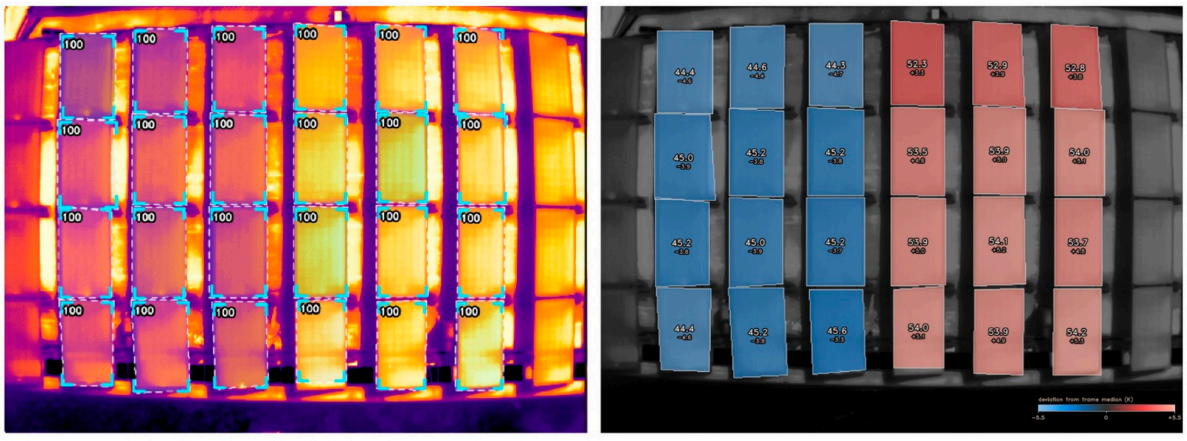


Figure 11. Module-level segmentation and radiometric verification stages of the pipeline applied to one aerial thermogram: (**a**) output of the segmentation model (**b**) median surface temperature of each module (°C) and its deviation (K) from the frame median, colour-coded from blue (cooler) to red (warmer).

The hotspot-detection stage of the pipeline is illustrated in Figure 12. Figure 12a presents the raw aerial thermogram of the array section affected by vegetation-cast shading, while Figure 12b shows the corresponding output of the detection model. The detections were produced by a YOLO-style single-stage object-detection model trained specifically for hotspot recognition. The model successfully localizes the cell-level thermal anomalies concentrated along the shaded edge of the array, assigning each detection a confidence score, with the identified hotspots detected at confidence levels ranging from 94% to 98%.

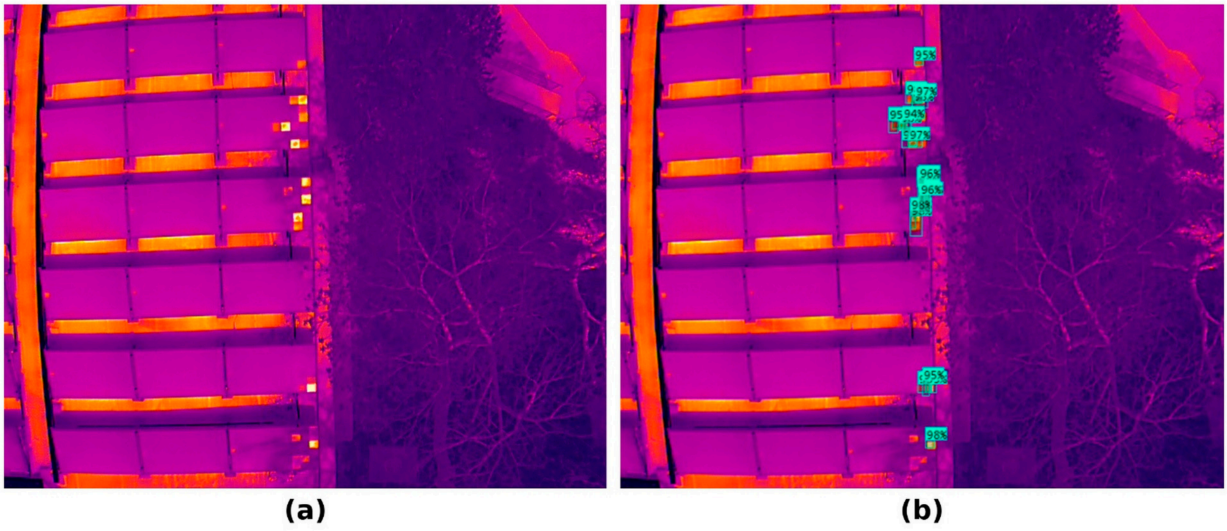


Figure 12. Hotspot-detection stage of the pipeline applied to the array section shaded by the adjacent vegetation: (**a**) raw radiometric aerial thermogram, in which the cell-level hotspots appear as bright spots along the array edge next to the tree canopy; (**b**) output of the YOLO-style single-stage detector trained for hotspot recognition, with each detected hotspot marked by a bounding box and its confidence score.

Any learned detector nevertheless exhibits a non-zero rate of false positives and false negatives, and the framework is therefore structured such that the detector operates as a screening stage rather than as the basis for maintenance decisions (Table 3). A false positive, a benign thermal signature arising from specular glare, transient shading or soiling that is classified as a module defect, would, in a detection-only workflow, result in an unnecessary site visit or, where misinterpreted as an intrinsic fault, an unnecessary module replacement. In the proposed framework, each candidate detection is subjected to radiometric verification against neighbouring electrically healthy strings, glare filtering, r.sun cast-shadow simulation at the acquisition timestamp, inspection of the co-registered RGB imagery and cross-referencing with SCADA data prior to any field action; a false positive is consequently rejected during analysis, at the cost of analyst time rather than field labour. The shading-induced hotspots reported in Section 3.4.2 exemplify this attribution process: in the absence of environmental context, these detections would have been reported as intrinsic module defects, whereas the combined r.sun and RGB evidence identified vegetation clearance, a considerably less costly corrective action, as the appropriate response. A false negative constitutes the more consequential error, since a defect that is not flagged cannot enter the verification chain and its cost accrues continuously until detected by other means—approximately 6088 kWh per year of forfeited production in the case of the open-circuited string (Section 3.4.1), together with accelerated degradation and elevated fire risk for hotspots sustaining temperatures in excess of 100 °C. This exposure is bounded by two detection paths that are independent of the object detector: the per-module radiometric median comparison (Figure 11b), which is applied to every segmented module irrespective of the detector output, and the per-region

SCADA analysis of Section 3.4.3, which reveals a production deficit even where the aerial survey fails to identify its cause, as demonstrated by the divergence between the MAC03 and MAC04 regions. Given the low cost of rejecting false positives within this framework, the detector may be operated at a conservative confidence threshold that favours recall over precision; a residual risk nonetheless remains for localized hotspots whose effect on power output is insufficient to be resolved in region-level SCADA data, and which can be recovered only through periodic re-survey.

Table 3. Consequences and cost drivers of detection errors in a detection-only workflow and in the proposed framework.

Error Type		Detection-Only Workflow	Proposed Framework
False positive	Consequence	Unnecessary site visit; possible unnecessary module replacement	Rejected before field action by radiometric, glare, *r.sun*, RGB and SCADA checks
	Cost driver	Field labour, travel, downtime, hardware	Analyst time per candidate detection
False negative	Consequence	Defect persists until the next scheduled inspection	Detected via radiometric median comparison or per-region SCADA deficit; targeted re-survey
	Cost driver	Lost yield × time to next inspection; degradation and safety risk	Lost yield × SCADA re-detection interval; residual risk for low-impact localized hotspots

3.3. Intervention

On 29 April, a corrective maintenance intervention was carried out at the photovoltaic installation with two principal objectives: the clearance of vegetation surrounding the array and the restoration of electrical continuity in a string exhibiting an open-circuit condition. The vegetation removal was performed to mitigate shading losses and to reduce the risk of soiling and physical obstruction of the modules, both of which are known to degrade energy yield and accelerate hotspot formation. Subsequently, the affected string was inspected and its connectors were re-seated in an attempt to re-establish the circuit. However, the open-circuit defect could not be resolved during this intervention, as the protective device at the bus bar power plug was triggered upon reconnection, interrupting the circuit and preventing the restoration of normal operation. This behaviour suggests that the fault is not attributable solely to a loose or degraded connection, but may instead originate from an underlying electrical anomaly, such as an insulation fault, a short circuit within the string, or a defective protection component. Further diagnostic investigation, including insulation resistance testing and I–V curve characterization, is therefore warranted before any subsequent corrective action is undertaken.

3.4. Root-Cause Attribution

The two anomaly classes that occurred on the installation are treated in turn in Sections 3.4.1 and 3.4.2, each following the full evidence chain of Algorithm 1. The electrical effect of the intervention is quantified in Section 3.4.3, and Section 3.4.4 reports the screening for the two remaining classes.

3.4.1. Open-Circuit Fault

The diagnostic investigation followed a progressive fault-localization methodology, proceeding from array-level indications to component-level identification. The anomaly was first detected as a thermal signature in the aerial thermographic survey, in which the affected string exhibited a temperature pattern inconsistent with that of the surrounding operational modules, indicative of a string not conducting current. The aerial thermographic evidence of the open-circuit defect is presented in Figure 13, processed with the DJI Thermal SDK (v1.4) to extract calibrated surface temperature measurements. The thermogram reveals that the modules of the affected string exhibit a distinctly elevated thermal

signature relative to the adjacent operational strings. This behaviour is characteristic of an open-circuited string.

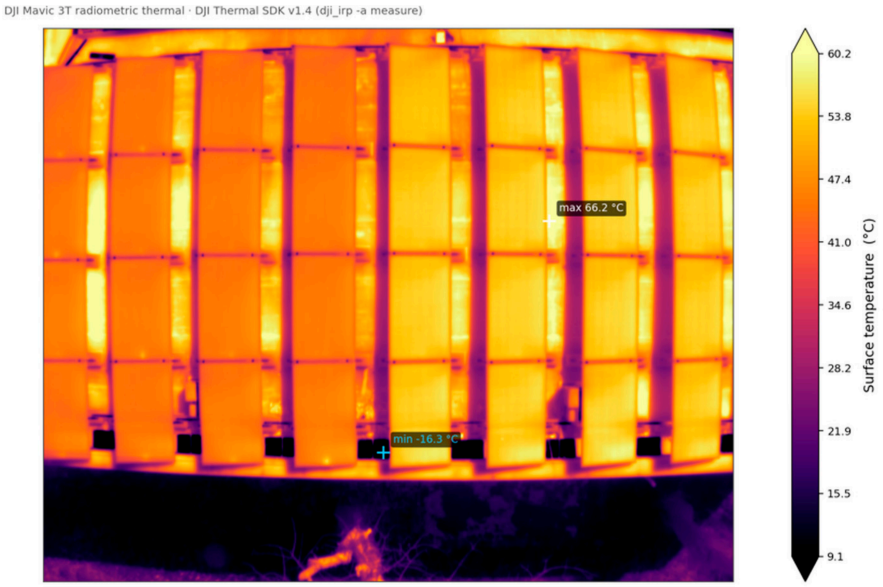


Figure 13. Radiometric aerial thermogram of the array acquired with a DJI Mavic 3T (DJI Thermal SDK v1.4), showing the uniformly elevated temperature of the open-circuited string in contrast with the adjacent operational strings.

This finding prompted a ground-based visual inspection of the array and its cabling, which revealed no evident mechanical damage, connector degradation, or shading-related cause, thereby directing attention toward the electrical balance of system. Subsequently, string-level electrical measurements were carried out at the combiner box, where the open-circuit voltage and current of the suspect string were compared against those of the healthy parallel strings; the suspect string presented a nominal open-circuit voltage but an absence of current under load, confirming a discontinuity downstream of the modules rather than a fault within the string itself. To localize the point of discontinuity, a handheld infrared thermographic inspection was then performed along the DC current path within the combiner and distribution enclosures, whereby the energized components displayed surface temperatures of up to approximately 40–43 °C, while one device exhibited no thermal signature consistent with current flow. This thermal contrast enabled the identification of the faulty circuit breaker, whose contact at the bus bar connection had been triggered into an open state, as the origin of the open-circuit defect.

The diagnostic procedure described above is illustrated in Figure 14. Subfigures (a) and (b) present the handheld infrared thermographic inspection performed along the DC current path, in which the energized conductors and terminals exhibit surface temperatures of up to approximately 40–43 °C, while the electrically inactive equipment displays no thermal signature consistent with current flow. Subfigure (c) shows the interior of the distribution enclosure, comprising the circuit breakers connected to the bus bar, among which the faulty breaker with the triggered bus bar contact was identified as the origin of the open-circuit defect.

To quantify the energy impact of the identified defect, a performance simulation was carried out using the PVWatts calculator developed by the National Renewable Energy Laboratory (NREL). The simulation modelled the production of the sixteen modules comprising the affected open-circuited string, taking into account the site's geographical location, the array's tilt and azimuth, and standard system loss assumptions. The results indicate that the estimated energy yield forfeited as a consequence of the string remaining out of operation

amounts to approximately 6088 kWh per year. This figure represents the annual production loss attributable to the open-circuit defect and underscores the economic and operational significance of restoring the string to service, thereby providing further justification for the prioritization of the corrective actions identified in the root-cause analysis.

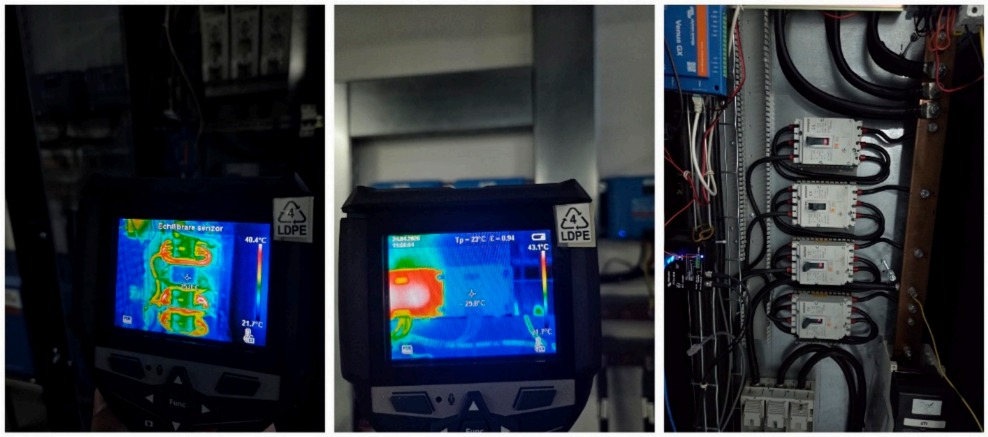


Figure 14. Thermographic and visual inspection of the DC distribution enclosure: (**a**,**b**) infrared thermal images of the current path showing energized components at 40.4 °C and 43.1 °C, respectively; (**c**) circuit breaker arrangement at the bus bar where the faulty breaker was identified.

The observations made during the intervention—nominal open-circuit voltage at the combiner, no current under load, and tripping of the protective device upon reconnection, suggest that the series path through the modules is intact and that closing the circuit produces a current that the protective device interprets as a fault. Three scenarios are consistent with this behaviour: (i) an insulation fault to earth within the string DC circuit (e.g., water ingress at a connector or junction box, cable abrasion, or backsheet damage); (ii) a partial short circuit manifesting only under load (e.g., a degraded bypass diode, a damaged inter-module cable, or a combiner wiring error); and (iii) a defective or under-rated protection component. These can be discriminated by a test sequence following IEC 62446-1 and IEC 61829. First, the insulation resistance between each pole and earth is measured with the string isolated; a value below the threshold of the standard points to scenario (i), and the fault can be localized by sectioning the string. Second, the open-circuit voltage (Voc) and short-circuit current (Isc), corrected to standard test conditions (STC), are measured and the I–V curve is traced; a reduced Voc, a step in the curve, or an anomalous slope near Voc or Isc points to scenario (ii). If both tests are nominal, the protective device is substituted and its ratings are verified against the string Voc and Isc in accordance with IEC 62548, which addresses scenario (iii). Restored operation can then be verified through the framework itself: string current at the combiner, region-level SCADA output relative to MAC04, and a repeat UAV thermographic survey.

3.4.2. Shading-Induced Hotspots

The occurrence of hotspot phenomena induced by partial shading is illustrated in Figure 15. The image was likewise acquired with the DJI Mavic 3T radiometric thermal sensor and processed using the DJI Thermal SDK (v1.4). In contrast to the uniform overheating pattern characteristic of the open-circuited string, this thermogram reveals localized, cell-level thermal anomalies concentrated along the edge of the array adjacent to the neighbouring vegetation, with peak surface temperatures reaching 109.9 °C. This behaviour is consistent with hotspot formation under partial shading conditions: when individual cells are shaded by the adjacent trees, they cease to generate current and are instead driven into reverse bias by the

unshaded cells of the same string, causing them to dissipate power as heat rather than produce it. The pronounced temperature differential between the affected cells and the surrounding module surface—exceeding 60 °C in places, indicates sustained localized heating, which over time can lead to accelerated encapsulant degradation, solder-bond fatigue, and permanent cell damage or even triggering a fire. These observations corroborate the necessity of the vegetation clearance performed during the 29 April intervention as a preventive measure against long-term shading-induced degradation.

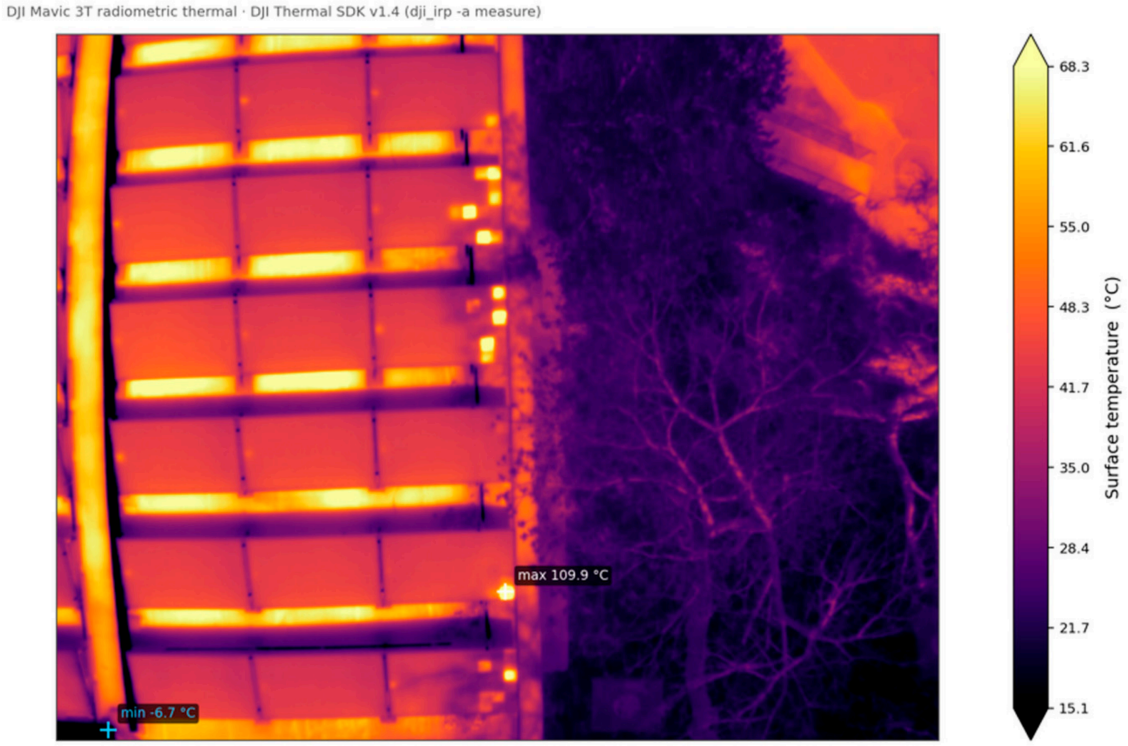


Figure 15. Radiometric aerial thermogram acquired with a DJI Mavic 3T (DJI Thermal SDK v1.4), showing cell-level hotspots (max. 109.9 °C) along the array edge caused by partial shading from adjacent vegetation.

In order to validate the anomalies identified during the aerial survey, a ground-based confirmation campaign was conducted at module level. The affected panels were subjected to a detailed visual inspection, which revealed partial shading of the module surface cast by the adjacent vegetation, together with the associated soiling and debris accumulation along the lower frame. Complementary to the visual assessment, thermal measurements were performed using a handheld infrared thermographic camera and additional measurement instrumentation, enabling the localization and quantification of the thermal anomalies at cell level. The ground thermogram, presented in Figure 16, confirms the presence of a pronounced hotspot with a peak surface temperature of 100.9 °C on the shaded module, against a background module temperature of approximately 31 °C, corroborating the shading-induced hotspot mechanism inferred from the aerial thermography. The corresponding photographic evidence illustrates the shadow pattern projected onto the module surface, establishing a direct causal correspondence between the observed shading condition and the measured thermal anomaly. This ground-level confirmation thereby substantiates the findings of the aerial survey and reinforces the diagnostic reliability of the combined aerial–terrestrial inspection methodology.

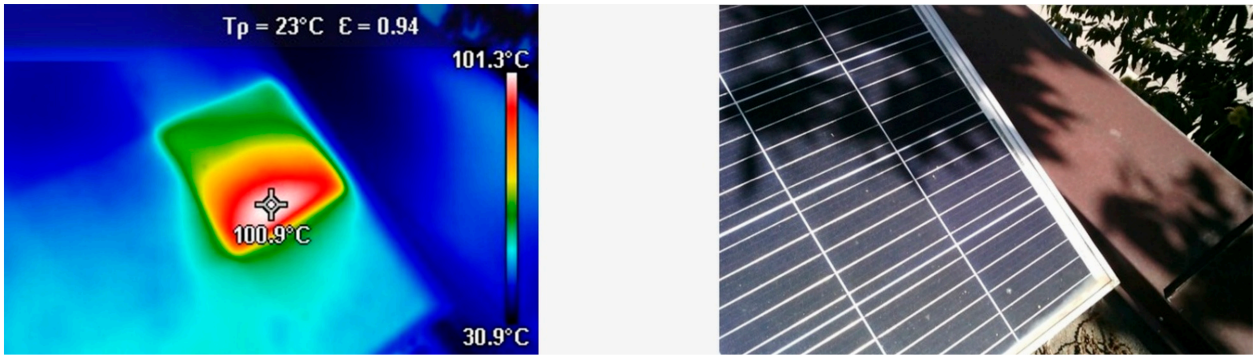


Figure 16. Ground-based confirmation of the shading-induced hotspot: (**left**) handheld infrared thermogram showing a localized hotspot of 100.9 °C; (**right**) photograph of the corresponding module showing the shadow cast by adjacent vegetation.

The temporal variability of shading conditions is illustrated in Figure 17, which presents two aerial thermograms of the same array section acquired on consecutive survey dates and at different times of day. A comparison of the two images reveals that the shadow patterns projected by the adjacent vegetation, and the associated cell-level hotspots along the array edge, differ markedly in position and extent between the two acquisitions, demonstrating that shading is an inherently transient phenomenon governed by the diurnal and seasonal trajectory of the sun. This transience poses a fundamental challenge for automated thermographic fault detection: a hotspot observed at a given instant may correspond either to a persistent module defect or to a momentary shading condition, and conversely, a shading-critical location may appear entirely unaffected if surveyed at an hour when the obstruction casts no shadow. To address this ambiguity, the proposed automated detection pipeline incorporates the r.sun solar radiation model, which computes the position of the sun and the resulting beam irradiance and cast-shadow geometry for any date and time, based on a DSM of the site including the surrounding obstructions. By simulating the expected shadow distribution at the exact timestamp of each thermographic acquisition, the pipeline is able to discriminate between shading-induced thermal anomalies and genuine module defects, and furthermore to identify locations subject to recurrent shading exposure irrespective of the survey time. The integration of r.sun thereby transforms the instantaneous thermographic snapshot into a temporally contextualized diagnosis, which in the present case study led all 14 hotspot regions to be attributed to vegetation shading rather than to module defects. Its effect on false-positive rates in general was not measured.

In addition to the field-based diagnostics, the shading conditions affecting the photovoltaic array were evaluated numerically using the r.sun solar radiation model implemented in GRASS GIS. The simulation was performed over a high-resolution DSM of the site, incorporating the surrounding obstructions (vegetation and adjacent structures), which enables the computation of the direct-beam irradiance component and the associated cast-shadow geometry as a function of solar position. The shadow distribution was extracted at representative time steps spanning the full diurnal solar cycle, corresponding to the beginning of the insolation period, mid-afternoon (15:00 h), and the end of the cycle (Figure 18). The resulting binary shading maps, in which black denotes cells receiving no direct-beam irradiance, reveal a strongly time-dependent shading regime. At the beginning of the cycle (Figure 18a), low solar elevation angles cause the surrounding obstacles to cast extensive shadow patterns across the module surface, and a comparably severe, azimuthally shifted shading configuration recurs towards the end of the cycle (Figure 18c). By contrast, at 15:00 h (Figure 18b) the array is almost entirely free of obstruction shading, with the panel surface receiving unimpeded direct-beam irradiance. The convergence of the r.sun shading analysis with the visual, thermographic inspections and object detections therefore substantiates recurrent partial shading

at the extremities of the solar cycle as a primary driver of the observed hotspot formation and the associated performance degradation.

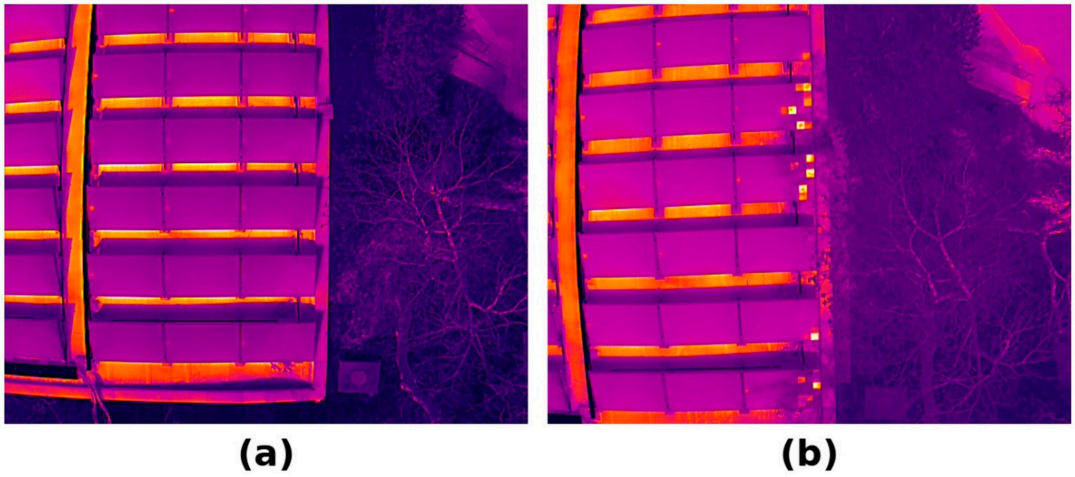


Figure 17. Aerial thermograms of the same array section acquired with the DJI Mavic 3T on (**a**) 17 April at 15:41 and (**b**) 18 April at 13:15, showing the displacement of the vegetation-cast shadow pattern and the appearance of edge-cell hotspots between acquisitions, illustrating the transient nature of shading. Dark purple corresponds to the lowest and bright yellow–white to the highest surface temperatures. The small bright spots along the right side of the rows in (**b**) indicate hotspots on individual cells. Cooler vegetation is visible to the right of the array.

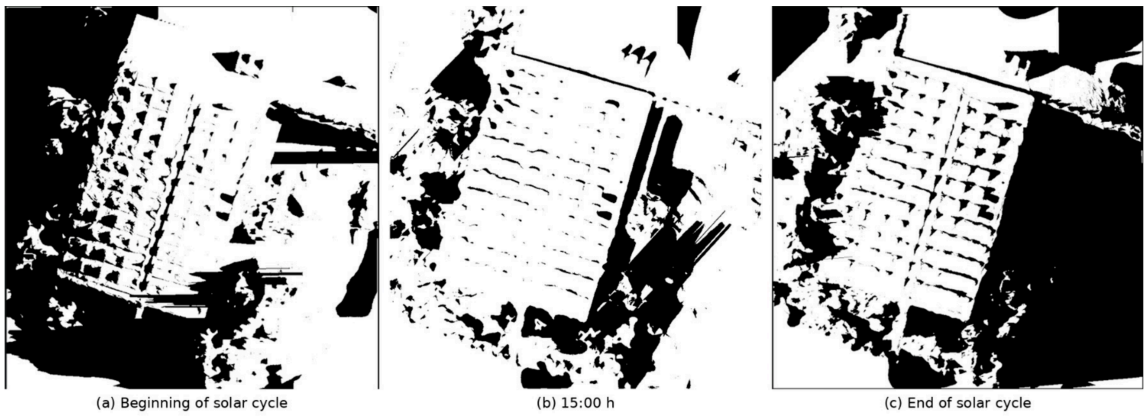


Figure 18. Binary cast-shadow maps of the photovoltaic array derived from the r.sun direct-beam irradiance simulation over the photogrammetric DSM, at (**a**) the beginning of the diurnal solar cycle, (**b**) 15:00 h, and (**c**) the end of the cycle (black = no direct-beam irradiance; white = illuminated surface).

A limitation of the present shading analysis lies in the origin of the DSM, which was derived from photogrammetric reconstruction rather than airborne light detection and ranging (LiDAR). Photogrammetric DSMs represent vegetation as closed, opaque volumes, whereas real canopies are partially permeable to direct-beam radiation, leading to a systematic overestimation of vegetation-cast shadows; fine-scale features such as branches are additionally smoothed or exaggerated, and no canopy penetration or foliage transmissivity can be modelled. The resulting binary shading maps should therefore be regarded as a conservative, worst-case estimate of the obstruction shading affecting the array, a constraint that could be addressed in future work through the acquisition of a UAV-LiDAR point cloud.

3.4.3. Weather-Matched Paired Analysis of SCADA Data

To separate a genuine change in plant behaviour from a change in the meteorological mix between the two observation windows, each daytime 30 min interval in the pre-period (29 March–28 April 2026, irradiance $\geq$ 50 W m^{-2}) was matched to the single most similar interval in the post-period (29 April–28 May 2026). Matching was performed as a nearest-neighbour search in a standardized four-dimensional covariate space, irradiance, ambient temperature, relative humidity and wind speed, subject to hard calipers (Table 4); pre-period intervals with no admissible partner were discarded rather than matched approximately, which trades sample size for the credibility of the "same weather" claim.

Table 4. Matching calipers and achieved covariate balance (n = 376 matched pairs).

Covariate	Caliper	Mean Absolute Within-Pair Residual
Irradiance	$\pm$25 W m^{-2}	12.6 W m^{-2}
Ambient temperature	$\pm$1.5 °C	0.76 °C
Relative humidity	$\pm$10%	4.6%
Wind speed	$\pm$1.2 m s^{-1}	0.35 m s^{-1}

Figure 19 plots every pair as a single point, pre-period power on the abscissa against its post-period twin on the ordinate, coloured by the irradiance of the pair, with the displacement widening as the points darken toward high irradiance.

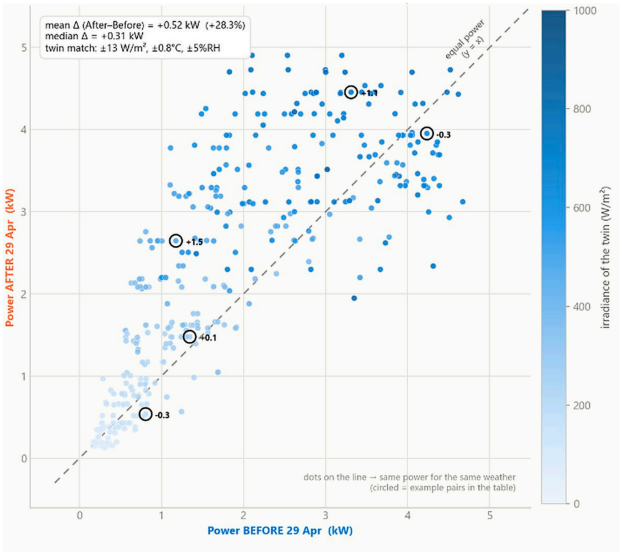


Figure 19. Weather-matched twin plot of power production before and after the intervention.

The distribution of paired differences is unimodal and displaced to the right of zero: 70% of pairs are positive, the mean is +0.518 kW and the median +0.310 kW, against a within-pair standard deviation of 0.858 kW that reflects the irreducible noise of comparing individual half-hours. The mean paired difference is +0.518 kW (95% CI +0.321 to +0.714 kW, day-clustered; t = 5.52, df = 19), equivalent to +28.3% of the 1.833 kW pre-period mean of the matched sample, the quantity attributable to the plant rather than to the weather. Stratification by irradiance (Table 5) shows the effect is not carried by any single regime:

Restricting the sample to pairs whose members both fall between 10:00 and 15:30, which removes the shoulder hours, where a small irradiance mismatch produces a large relative power error and where the solar-geometry difference between matched intervals is greatest, leaves n = 163 pairs and raises the absolute estimate to +0.686 kW (95% CI +0.471 to +0.902 kW, day-clustered on pre-day $\times$ post-day; t = 6.80, df = 15, $p = 6.0 \times 10^{-6}$). Measured against the correspondingly higher pre-period mean of 2.837 kW this is +24.2%,

marginally below the +28.3% of the full sample: the larger absolute gap tracks the larger output rather than a proportionally stronger midday effect. Twenty of the 25 pre-period days remain positive under the restriction (sign test $p = 4.1 \times 10^{-3}$), and the within-day dependence is weaker here than in the full sample (design effect 1.20 against 2.06), so the finding is a genuine high-output phenomenon and not an artefact of low-light matching.

Table 5. Paired difference by irradiance band.

Irradiance Band (W m^{-2})	Mean ΔP (kW)
50–200	+0.04 ± 0.04
200–350	+0.45 ± 0.12
350–500	+0.95 ± 0.23
500–650	+0.65 ± 0.19
>650	+0.81 ± 0.35

Applying the identical procedure to the co-located MAC04 inverter, which shares the meteorological instrumentation, yields a mean of −0.190 kW with a confidence interval spanning zero (−0.392 to +0.011 kW; 46% of pairs positive) and a midday mean of −0.595 kW (−0.960 to −0.230): MAC04 shows no comparable gain and, if anything, a small decline. This asymmetry is the decisive control, since any common-mode driver: pyranometer drift, a recalibration, or the seasonal rise in solar elevation that increases plane-of-array irradiance for a given horizontal-plane reading, would have displaced both units in the same direction.

Figure 20 presents the power response of the photovoltaic system as a function of solar irradiance, comparing the period before the intervention (29 March–28 April) with the period after it (29 April–28 May). In both cases, the 30 min mean output increases approximately linearly with irradiance up to around 650 W m^{-2}, beyond which the curves flatten. However, the post-intervention curve exhibits a consistently steeper slope, indicating that the system delivers more power per unit of irradiance across the entire operating range. At high irradiance levels, the "after" period reaches approximately 4 kW compared to roughly 3.2 kW beforehand—an improvement of about 25%—while remaining below the 5 kW inverter limit. The shaded inter-quartile bands overlap only partially, suggesting that the observed improvement is systematic rather than attributable to day-to-day variability.

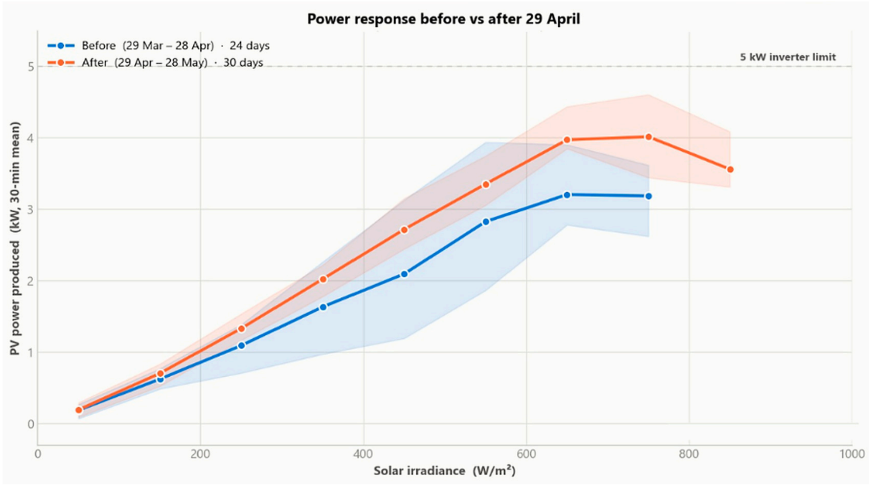


Figure 20. Power–irradiance curves before and after the intervention.

3.4.4. Screening for Bypassed Substrings and PID

The per-module radiometric analysis (Step 3c of Algorithm 1) and the manual interpretation of the aerial thermograms were also used to screen the 81 modules of PV 1 for the

two remaining classes of Section 2.4. No module showed the uniform heating of one-third or two-thirds of its surface that marks a conducting bypass diode, and no string showed the edge or corner heating repeated along consecutive modules that marks PID. The influence of bypassed substrings and PID on the studied arrays during the monitoring period was therefore nil, and the results of Sections 3.4.1–3.4.3 are not confounded by either effect.

Thermography is the only practical route to these two classes at the scale of the monitored regions. One bypassed substring removes about 110 W of a 330 Wp module, which is 1.9% of the installed capacity of MAC03 and 0.5% of that of MAC04. This is far below the within-pair standard deviation of 0.858 kW in the matched analysis of Section 3.4.3 and cannot be resolved in region-level SCADA data. PID develops over months or years and would appear in SCADA data as a gradual decline in the output of the affected string and not as a step change, so that the 77-day monitoring period is too short to reveal it electrically.

Had either signature been present, it would have been processed as follows. A bypassed substring that is shading-confirmed in Step 5 is treated as reversible: the obstruction is removed and the module is re-surveyed. One that is unshaded, or that persists in a frame acquired when the shaded fraction is zero, is referred under rule 7a to field verification by bypass-diode test and I–V curve tracing. A PID candidate is checked against the string layout, since PID typically concentrates in the modules at the negative end of the string, and is then referred to I–V curve tracing and insulation resistance measurement, with the long-term SCADA trend of the region as supporting evidence. These steps describe the procedure and were not exercised in this study.

3.5. Ground-Truth Events and Summary of Diagnostic Outcomes

The evaluation rests on a single installation and on a small number of ground-truth events. Table 6 sets the four anomaly classes considered in the framework (Section 2.4) against the events that actually occurred on the 81-module PV 1 array. Two classes occurred: one open-circuited string of 16 modules and 14 hotspot regions, all of which were traced to vegetation shading. No intrinsic cell-level hotspot, bypassed substring, or PID signature was observed (Section 3.4.4). The ground truth therefore comprises 15 events arising from two physical causes. The survey of PV 2 served only to test the acquisition and processing workflow on a different array configuration and contributes no ground-truth events to the results reported here.

Table 6. Anomaly classes considered in the framework and ground-truth events that occurred on the PV 1 installation (81 modules).

Anomaly Class Considered (Section 2.4)	Events That Occurred on PV 1	Ground-Truth Verification	Cause Established
Hotspot	14 regions	Handheld infrared thermography and visual inspection; r.sun simulation and RGB imagery	Vegetation shading (all 14); no intrinsic cell-level hotspot observed
Bypassed substring	0	Not applicable	Not applicable
PID	0	Not applicable	Not applicable
Open-circuit fault	1 string (16 modules)	String-level voltage and current measurements at the combiner box; handheld infrared thermography of the DC distribution enclosure	Open protection device at the bus bar; underlying electrical cause unresolved
Total: 4 classes	15 events in 2 classes		2 physical causes

This has consequences for the interpretation of the results. The agreement reported in Section 3.2 (15 of 15 events) cannot be read as a detection rate, and the absence of unconfirmed detections cannot be read as a false-alarm rate. The identification of bypassed substrings and PID, and the separation of intrinsic from shading-induced hotspots when both are present, were not tested. The quantitative result that carries statistical weight is the weather-matched SCADA analysis of Section 3.4.3, which rests on 376 matched intervals rather than on the number of defects and applies to the MAC03 region and to the intervention carried out there.

Table 7 sets the results of the case study against the four diagnostic levels defined in Section 2.7, together with the metric applied at each level and the aspects that were not established.

Table 7. Diagnostic levels, evaluation metrics, and outcomes obtained in the case study.

Diagnostic Level	Evaluation Metric	Outcome in the Case Study	Not Established
Level 1: detection and localization	Agreement between automated detections and the reference set from manual aerial interpretation and ground inspection (reference anomalies detected and missed; detections not confirmed)	Open-circuited string: 1 of 1 detected. Hotspot regions: 14 detected, all 14 confirmed by ground thermography. No reference anomaly missing from the automated output (Section 3.2).	Precision, recall, and cross-site generalization of the detection models
Level 2: fault-type identification and root-cause attribution	Confirmation of the image-based class by independent evidence: radiometric comparison with healthy strings, r.sun and RGB shading analysis, string-level electrical measurements, ground thermography	Open-circuit class confirmed by nominal open-circuit voltage and absence of current under load at the combiner box; discontinuity localized to a circuit breaker at the bus bar (Section 3.4.1). Hotspots attributed to vegetation shading by r.sun, RGB imagery, and ground thermography (100.9 °C on the shaded module) (Section 3.4.2).	Cause of the protective-device tripping on reconnection (insulation fault, partial short circuit, or defective protection component). Only the hotspot and open-circuit classes were exercised.
Level 3: severity quantification	Temperature difference ΔT relative to a healthy reference under the same irradiance; estimated energy loss	Open-circuited string: up to +5.3 K above the frame median (52–54 °C against 44–46 °C); approximately 6088 kWh per year (PVWatts, 16 modules). Hotspots: peak 109.9 °C, more than 60 °C above the surrounding module surface.	Electrical loss attributable to individual hotspots, which is not resolvable in region-level SCADA data. Prognosis is out of scope.
Level 4: maintenance decision support	Corrective action selected from Levels 1–3; weather-matched change in power after the intervention with 95% CI, compared with a co-located control sub-array	Vegetation clearance selected instead of module replacement; follow-up test sequence defined for the open-circuited string. MAC03: +0.518 kW (95% CI 0.321–0.714 kW; +28.3%); midday +0.686 kW (0.471–0.902 kW; +24.2%). MAC04 control: −0.190 kW (−0.392 to +0.011 kW) (Section 3.4.3).	Performance recovery after restoration of the open-circuited string. Economic ranking of maintenance actions.

Levels 1 and 2 were satisfied for both anomaly types as far as fault class and location are concerned, whereas the cause of the protective-device tripping on reconnection of the open-circuited string remains to be determined. At Level 3, severity was quantified thermally for both anomaly types and electrically for the open-circuited string only. At Level 4, the effect of the intervention was verified for the MAC03 region against the MAC04 control, while the recovery obtainable from restoring the open-circuited string could not yet be measured.

4. Limitations and Scope of Applicability

The framework was developed and demonstrated on one rooftop installation, and its transfer to other installations depends on the factors discussed below. For each factor, the elements of the method that are site-specific and those that carry over unchanged are indicated.

Scope of the case study. The case study comprises an 81-module installation on which two of the four anomaly classes occurred. The steps of Algorithm 1 that concern bypassed substrings, PID, and intrinsic hotspots follow the same evidence chain but remain to be exercised on installations where these classes are present. The decision thresholds of Table A1 were chosen for this site and sensor and should be treated as starting values to be confirmed at a new site. The quantitative evaluation of the detection models is the subject of a separate study.

PV technology and module construction. The modules studied are monocrystalline silicon modules of 330–360 Wp, and the workflow itself is independent of cell technology. Two elements are technology-dependent. First, the temperature rise of an open-circuited module over its operating neighbours scales with module efficiency, so the margin of +3 to +5.3 K observed here is expected to be somewhat smaller for polycrystalline or thin-film modules, and the module-level threshold should be adjusted accordingly. Second, the class rules of Step 4 are written for full-cell modules with three bypass diodes and need to be adapted to the substring layout of half-cut, shingled, or thin-film modules. Encapsulant-related degradation such as discolouration or delamination is not part of the present taxonomy; where it is suspected, the thermal survey is best complemented by electroluminescence imaging or I–V measurements.

Mounting geometry and vegetation. The arrays studied are mounted at a fixed tilt of 15° on flat rooftops, with trees beside the roof edge as the only obstruction. The photogrammetric DSM represents canopies as opaque volumes and therefore gives a conservative estimate of vegetation shadows (Section 3.4.2), which was sufficient to attribute the hotspots in this study. For ground-mounted arrays with low clearance, low vegetation in front of the first module row and row-to-row shading at low sun become relevant and are resolved less well by a DSM of this kind. Because vegetation changes with season and maintenance, the DSM should be re-acquired at each survey, which the workflow already does by reconstructing it from the RGB images of the same flight. UAV-LiDAR would further improve the representation of canopies.

Climate and wind. The campaign covered a temperate-continental late spring with calm conditions at a sheltered rooftop (wind below 3 m s^{-1} in 98% of daytime bins). Wind reduces the temperature contrast of thermal signatures through convective cooling, so at exposed sites the thresholds should be confirmed under local conditions, within the acquisition limits of IEC TS 62446-3 that the protocol already applies. In winter or at high latitudes the irradiance condition for flights is met less often, which restricts the inspection calendar and not the method. The weather-matched analysis relies on comparable weather before and after an intervention; where the two periods differ strongly, fewer intervals are matched and a longer observation window is needed.

UAV flight parameters and camera characteristics. All flights used one platform (DJI Mavic 3T; 640 × 512 pixel uncooled microbolometer) at constant altitude, speed, overlap, and nadir view. Flight altitude determines the ground sampling distance. String-level faults are robust to it, whereas cell-level hotspots require the resolution recommended by IEC TS 62446-3 (at least 5 × 5 pixels per cell) if their ΔT is not to be underestimated. Flight speed and image overlap should likewise stay within the ranges that avoid thermal smearing and preserve the quality of the DSM. On steeper arrays or trackers reflections increase, and the glare criterion becomes more important. Because uncooled microbolometers are more accurate in relative than in absolute terms, Algorithm 1 relies on temperature differences

within a frame, an approach that carries over to other cameras; the numerical thresholds and the detection models should nevertheless be recalibrated for a different sensor. A single flight records one shadow configuration (Figure 17), which is why the diurnal r.sun simulation is part of the workflow.

Electrical monitoring. Electrical evidence was available as AC power for two independently metered regions. This resolves string-level faults and the effect of the intervention, but not small defects such as single hotspots (Section 3.4.4); string-level monitoring, where installed, would extend the SCADA test of Step 6 to smaller faults. I–V curve tracing was not part of this campaign and is identified as the next diagnostic step for the open-circuited string.

5. Conclusions

This study presented an integrated framework for photovoltaic fault diagnosis that combines UAV-based radiometric thermography and RGB imaging with SCADA telemetry, meteorological monitoring, DSM-based solar-radiation modelling, automated anomaly detection, and targeted ground-level verification. The proposed approach extends conventional aerial thermographic inspection beyond anomaly localization by incorporating the environmental and electrical context required to distinguish transient operating effects from faults with direct consequences for system performance.

The experimental investigation demonstrated the complementary value of the different diagnostic layers. UAV thermography identified both a string-level open-circuit condition and localized hotspots associated with vegetation-induced partial shading. The open-circuited string exhibited a uniform thermal elevation of approximately 52–54 °C compared with 44–46 °C for normally operating modules, while shading-induced hotspots reached a maximum aerial temperature of 109.9 °C. Ground-based inspection confirmed the hotspot mechanism, with a measured peak temperature of 100.9 °C, and linked the anomaly directly to vegetation shading. In parallel, electrical and thermographic investigation of the DC distribution system localized the open-circuit condition to the protection and bus bar connection path. The unsuccessful attempt to restore the affected string during the maintenance intervention further indicated that additional electrical investigation is required before the string can be safely returned to operation.

An important outcome of the study is the demonstration that environmental context is essential for reliable interpretation of aerial thermal anomalies. The integration of RGB observations and DSM-based *r.sun* simulations showed that vegetation shading varies substantially with solar position and acquisition time. Consequently, an isolated thermographic observation may otherwise lead to incorrect attribution of a transient shading-induced hotspot to an intrinsic module defect. Incorporating spatial shading information therefore provides a mechanism for reducing environmentally induced misattribution, although the size of this effect cannot be quantified from a single installation.

The SCADA-based weather-matched analysis provided quantitative evidence of a change in electrical performance following the intervention. Using 376 matched pre- and post-intervention 30 min intervals with comparable irradiance, ambient temperature, relative humidity, and wind speed, the investigated MAC03 region exhibited a mean power difference of +0.518 kW (95% CI: +0.321 to +0.714 kW), corresponding to a 28.3% increase relative to the matched pre-intervention mean. Restricting the analysis to the 10:00–15:30 high-output period resulted in a mean difference of +0.686 kW (95% CI: +0.471 to +0.902 kW; $p = 6.0 \times 10^{-6}$), equivalent to 24.2%. In contrast, the co-located MAC04 region showed no comparable positive response, strengthening the interpretation that the observed MAC03 improvement was not primarily driven by common meteorological or seasonal effects.

For the two fault types encountered, no single diagnostic source was sufficient for a complete assessment. UAV thermography provides rapid spatial localization, RGB imagery

and solar modelling establish environmental context, SCADA data quantify operational consequences, and field measurements enable physical root-cause verification. Their integration into a unified workflow therefore provides a more robust basis for condition-based maintenance and maintenance prioritization than thermographic inspection or electrical monitoring used independently.

These findings come from a single-installation case study with 15 ground-truth events in two of the four anomaly classes considered. The detection results demonstrate the feasibility of the approach, and its general performance remains to be established on further sites. The statistically supported result is the weather-matched SCADA analysis, which rests on 376 matched intervals. The scope of applicability of the method is discussed in Section 4.

Future work should focus on validating the framework across larger and more diverse PV installations, quantitatively evaluating the automated detection models in terms of precision, recall, and cross-site generalization, and improving shading representation through higher-fidelity three-dimensional data such as UAV-LiDAR. In particular, a multi-site dataset with a sufficient number of verified events in each anomaly class, including bypassed substrings and PID, which did not occur on the studied arrays, will be used to assess the detection accuracy for thermographic candidates, the identification accuracy for fault type, the reduction in false positives obtained from environmental context, and the performance of the framework relative to thermography-only, SCADA-only, DSM-only, and simplified-threshold baselines. The present single-installation case study does not support such estimates. A further direction concerns the detection stage itself. The models used here were treated as a fixed screening component; future work will compare alternative object-detection architectures, including newer YOLO generations, transformer-based detectors, and oriented-bounding-box variants [41], on the multi-site dataset, with particular attention to recall for small cell-level hotspots and to inference speed. This comparison is also a prerequisite for coupling detection to flight planning. In the present study all flights followed pre-programmed routes and the targeted re-survey of Step 7c was scheduled manually, whereas in an autonomous inspection scheme, near-real-time detections would trigger adaptive re-routing, for example a lower-altitude pass over a flagged module to reach the cell-level resolution. Because a missed detection generates no follow-up waypoint, the detection rate of the model directly bounds the effectiveness of such routing, and the detector-independent radiometric and SCADA paths of the framework would remain necessary as a safeguard. Further electrical characterization of the unresolved open-circuit string, including insulation resistance testing and I–V curve analysis, is also required to determine the underlying electrical fault and quantify the performance recovery achievable after its complete restoration.

Author Contributions: Conceptualization, G.C. and T.L.; methodology, T.L., G.C. and C.I.; software, T.L. and C.I.; validation, T.L., A.P.U. and G.C.; formal analysis, T.L. and C.I.; investigation, T.L. and A.P.U.; resources, H.N., G.C. and L.T.G.; data curation, T.L. and C.I.; writing—original draft preparation, T.L.; writing—review and editing, G.C., H.N., L.T.G., C.I. and A.P.U.; visualization, T.L. and A.P.U.; supervision, H.N. and L.T.G.; project administration, G.C. and H.N.; funding acquisition, H.N. and L.T.G. All authors have read and agreed to the published version of the manuscript.

Funding: This research received no external funding.

Data Availability Statement: The original contributions presented in this study are included in the article. Further inquiries can be directed to the corresponding author.

Acknowledgments: The authors gratefully acknowledge the contribution of the European Union's Horizon 2020 research and innovation program, under grant agreement No 857801—"Smart and local ReneWable Energy DISTRICT heating and cooling solutions for sustainable living"—WEDISTRICT to the development of the research infrastructure used in this study. Although the present research benefited from this infrastructure, the project had been completed before the preparation and submission of this manuscript and did not provide financial support for the publication of this work.

Conflicts of Interest: The authors declare no conflicts of interest.

Appendix A

Table A1. Parameters of the diagnostic pipeline (Algorithm 1).

Parameter	Symbol	Value	Step
Minimum in-plane irradiance for a flight	G_{min}	600 W m^{-2}	1
Maximum wind speed for a flight	v_{max}	20 km h^{-1}	1
Thermal sensor and radiometric extraction		640 × 512 px, 8–14 µm; DJI Thermal SDK v1.4	2, 3
Photogrammetry and solar modelling software		OpenDroneMap v3.6.0 GRASS GIS v8.5.0 r.sun	2, 5
DSM resolution	r_{DSM}	0.10 m	2, 5
Detector confidence threshold	τ_c	90% (hotspot detections in this study: 94–98%)	3b
Glare criterion		Bright region with low local variance or low Laplacian or U-net trained on glare masks	3b
Module-level temperature threshold	ΔT_{mod}	2 K (open-circuited string in this study: +3 to +5.3 K above the frame median)	3c
Cell-level temperature threshold	ΔT_{cell}	10 K (hotspots in this study: more than 60 °C above the surrounding surface)	3c
r.sun shadow criterion	S	Direct-beam irradiance = 0 at the frame timestamp	5
SCADA aggregation		30 min bins; daytime floor 20 W m^{-2}	6, 10
Irradiance floor for deficit and matching	G_{match}	50 W m^{-2}	6, 10
Deficit tolerance	δ	5% of installed capacity	6
Energy-loss model		PVWatts (NREL), standard system-loss assumptions	9
Matching calipers		± 25 W m^{-2} irradiance; ± 1.5 °C ambient temperature; ± 10% relative humidity; ± 1.2 m s^{-1} wind speed	10
Matching and inference		Nearest neighbour in standardized four-dimensional space; unmatched bins discarded; day-clustered 95% confidence interval; co-located control region	10

Table A2. UAV acquisition and thermal camera parameters.

Parameter	Value
UAV platform	DJI Mavic 3T
Thermal sensor	Uncooled VOx microbolometer, 640 × 512 px, 12 µm pixel pitch, 8–14 µm
Thermal lens	Diagonal field of view 61°, 40 mm equivalent focal length, f/1.0
Thermal sensitivity and accuracy (manufacturer)	Noise-equivalent temperature difference ≤ 50 mK; ± 2 °C or ± 2%, whichever is larger
Thermal image format	Radiometric JPEG (R-JPEG), 16-bit; temperatures extracted with DJI Thermal SDK v1.4
RGB camera	1/2-inch CMOS, 48 MP, 24 mm equivalent focal length
Route altitude	22.7 m (74.6 ft, as set in DJI Pilot 2)
Thermal ground sampling distance	3.0 cm px^{-1}
RGB ground sampling distance	Below 1 cm px^{-1}
Flight speed	1.3 m s^{-1} (3 mph)
Forward/side image overlap	75%/85%
Viewing geometry	Nadir
Emissivity	0.95

References

1. International Energy Agency (IEA). Renewables 2024: Analysis and Forecast to 2030. Available online: https://www.iea.org/reports/renewables-2024 (accessed on 10 February 2026).
2. Jäger-Waldau, A. Snapshot of photovoltaics—March 2025. *EPJ Photovolt.* **2025**, *16*, 22. [CrossRef] [PubMed]

3. Chatzipanagi, A.; Jaeger-Waldau, A.; Letout, S.; Mountraki, A.; Gea Bermudez, J.; Georgakaki, A.; Ince, E.; Schmitz, A. *Clean Energy Technology Observatory: Photovoltaics in the European Union—2025 Status Report on Technology Development, Trends, Value Chains and Markets*; Publications Office of the European Union: Luxembourg, 2025. [CrossRef]
4. Green, M.A.; Dunlop, E.D.; Yoshita, M.; Kopidakis, N.; Bothe, K.; Siefer, G.; Hao, X.; Jiang, J.Y. Solar cell efficiency tables (Version 66). *Prog. Photovolt. Res. Appl.* **2025**, *33*, 795–810. [CrossRef]
5. Fraunhofer Institute for Solar Energy Systems ISE. Photovoltaics Report Updated 2025. Available online: https://www.ise.fraunhofer.de/en/publications/studies/photovoltaics-report.html (accessed on 23 July 2026).
6. International Renewable Energy Agency. Renewable Power Generation Costs in 2023 International Renewable Energy Agency. 2024. Available online: https://www.irena.org/Publications/2024/Sep/Renewable-Power-Generation-Costs-in-2023 (accessed on 23 July 2026).
7. Aghaei, M.; Fairbrother, A.; Gok, A.; Ahmad, S.; Kazim, S.; Lobato, K.; Oreski, G.; Reinders, A.; Schmitz, J.; Theelen, M.; et al. Review of degradation and failure phenomena in photovoltaic modules. *Renew. Sustain. Energy Rev.* **2022**, *159*, 112160. [CrossRef]
8. International Electrotechnical Commission. *IEC TS 63209-1:2021—Extended-Stress Testing of Photovoltaic Modules for Longer Service Life—Part 1: Modules*; IEC: Geneva, Switzerland, 2021.
9. Straub-Mück, M.; Geyer-Klingeberg, J.; Rathgeber, A.W. Determinants of the long-term degradation rate of photovoltaic modules: A meta-analysis. *Renew. Sustain. Energy Rev.* **2025**, *216*, 115697. [CrossRef]
10. Kempe, M.D. Modeling of rates of moisture ingress into photovoltaic modules. *Sol. Energy Mater. Sol. Cells* **2006**, *90*, 2720–2738. [CrossRef]
11. Köntges, M.; Kurtz, S.; Packard, C.; Jahn, U.; Berger, K.A.; Kato, K.; Friesen, T. *Review of Failures of Photovoltaic Modules*; IEA PVPS Task 13 Report T13-01; IEA: Paris, France, 2014.
12. Mellit, A.; Tina, G.M.; Kalogirou, S.A. Fault detection and diagnosis methods for photovoltaic systems: A review. *Renew. Sustain. Energy Rev.* **2018**, *91*, 1–17. [CrossRef]
13. Daliento, S.; Chouder, A.; Guerriero, P.; Massi Pavan, A.; Mellit, A.; Moeini, R.; Tricoli, P. Monitoring, Diagnosis, and Power Forecasting for Photovoltaic Fields: A Review. *Int. J. Photoenergy* **2017**, *2017*, 1356851. [CrossRef]
14. Tsanakas, J.A.; Ha, L.; Buerhop, C. Faults and infrared thermographic diagnosis in operating c-Si photovoltaic modules: A review of research and future challenges. *Renew. Sustain. Energy Rev.* **2016**, *62*, 695–709. [CrossRef]
15. Aghaei, M.; Dolara, A.; Leva, S.; Grimaccia, F. Image resolution and defects recognition in photovoltaic modules and solar plants: Application of unmanned aerial vehicles. *Energy Procedia* **2017**, *134*, 136–148. [CrossRef]
16. Silvestre, S.; da Silva, M.A.; Chouder, A.; Guasch, D.; Karatepe, E. New procedure for fault detection in grid connected PV systems based on the evaluation of current and voltage indicators. *Energy Convers. Manag.* **2014**, *86*, 241–249. [CrossRef]
17. Gallardo-Saavedra, S.; Hernández-Callejo, L.; Duque-Perez, O. Technological review of the instrumentation used in aerial thermographic inspection of photovoltaic plants. *Renew. Sustain. Energy Rev.* **2018**, *93*, 566–579. [CrossRef]
18. Pruthviraj, U.; Kashyap, Y.; Baxevanaki, E.; Kosmopoulos, P. Solar photovoltaic hotspot inspection using unmanned aerial vehicle thermal images at a solar field in South India. *Remote Sens.* **2023**, *15*, 1914. [CrossRef]
19. International Electrotechnical Commission. *IEC TS 62446-3:2017. Photovoltaic (PV) Systems—Requirements for Testing, Documentation and Maintenance—Part 3: Photovoltaic Modules and Plants—Outdoor Infrared Thermography*; IEC: Geneva, Switzerland, 2017.
20. Buerhop, C.; Bommes, L.; Schlipf, J.; Pickel, T.; Fladung, A.; Peters, I.M. Infrared imaging of photovoltaic modules: A review of the state of the art and future challenges facing gigawatt photovoltaic power stations. *Prog. Energy* **2022**, *4*, 042010. [CrossRef]
21. Badea, G.P.; Frigioescu, T.F.; Dombrovschi, M.; Cican, G.; Dima, M.; Anghel, V.; Crunteanu, D.E. Innovative Hybrid UAV Design, Development, and Manufacture for Forest Preservation and Acoustic Surveillance. *Inventions* **2024**, *9*, 39. [CrossRef]
22. Zefri, Y.; Sebari, I.; Hajji, H.; Aniba, G. Developing a deep learning-based layer-3 solution for thermal infrared large-scale photovoltaic module inspection from orthorectified big UAV imagery data. *Int. J. Appl. Earth Obs. Geoinf.* **2022**, *106*, 102652. [CrossRef]
23. Bommes, L.; Hoffmann, M.; Buerhop-Lutz, C.; Pickel, T.; Hauch, J.; Brabec, C.; Maier, A.; Peters, I.M. Anomaly detection in IR images of PV modules using supervised contrastive learning. *Prog. Photovolt. Res. Appl.* **2022**, *30*, 597–614. [CrossRef]
24. Triki-Lahiani, A.; Bennani-Ben Abdelghani, A.; Slama-Belkhodja, I. Fault detection and monitoring systems for photovoltaic installations: A review. *Renew. Sustain. Energy Rev.* **2018**, *82*, 2680–2692. [CrossRef]
25. Hijjawi, U.; Lakshminarayana, S.; Xu, T.; Malfense Fierro, G.P.; Rahman, M. A review of automated solar photovoltaic defect detection systems: Approaches, challenges, and future orientations. *Sol. Energy* **2023**, *266*, 112186. [CrossRef]
26. Deitsch, S.; Christlein, V.; Berger, S.; Buerhop-Lutz, C.; Maier, A.; Gallwitz, F.; Riess, C. Automatic classification of defective photovoltaic module cells in electroluminescence images. *Sol. Energy* **2019**, *185*, 455–468. [CrossRef]
27. El-Banby, G.M.; Moawad, N.M.; Abouzalm, B.A.; Abouzaid, W.F.; Ramadan, E.A. Photovoltaic system fault detection techniques: A review. *Neural Comput. Appl.* **2023**, *35*, 24829–24842. [CrossRef]

28. Kandeal, A.W.; Elkadeem, M.R.; Thakur, A.K.; Abdelaziz, G.B.; Sathyamurthy, R.; Kabeel, A.E.; Yang, N.; Sharshir, S.W. Infrared thermography-based condition monitoring of solar photovoltaic systems: A mini review of recent advances. *Sol. Energy* **2021**, *223*, 33–43. [CrossRef]
29. Michail, A.; Livera, A.; Tziolis, G.; Carús Candás, J.L.; Fernandez, A.; Antuña Yudego, E.; Fernández Martínez, D.; Antonopoulos, A.; Tripolitsiotis, A.; Partsinevelos, P.; et al. A comprehensive review of unmanned aerial vehicle-based approaches to support photovoltaic plant diagnosis. *Heliyon* **2024**, *10*, e23983. [CrossRef] [PubMed]
30. Aghaei, M.; Kolahi, M.; Nedaei, A.; Venkatesh, N.; Esmailifar, S.; Moradi Sizkouhi, A.; Aghamohammadi, A.; Oliveira, A.; Eskandari, A.; Parvin, P.; et al. Autonomous Intelligent Monitoring of Photovoltaic Systems: An In-Depth Multidisciplinary Review. *Prog. Photovolt. Res. Appl.* **2025**, *33*, 381–409. [CrossRef]
31. Kolahi, M.; Esmailifar, S.M.; Moradi Sizkouhi, A.M.; Aghaei, M.; Rüther, R. Digital-PV: A digital twin-based platform for autonomous aerial monitoring of large-scale photovoltaic power plants. *Energy Convers. Manag.* **2024**, *321*, 118963. [CrossRef]
32. Lindig, S.; Herz, M.; Ascencio-Vásquez, J.; Theristis, M.; Herteleer, B.; Deckx, J.; Anderson, K. Review of technical photovoltaic key performance indicators and the importance of data quality routines. *Sol. RRL* **2024**, *8*, 2400634. [CrossRef]
33. Wang, Q.; Paynabar, K.; Pacella, M. Online automatic anomaly detection for photovoltaic systems using thermography imaging and low rank matrix decomposition. *J. Qual. Technol.* **2022**, *54*, 503–516. [CrossRef]
34. de Oliveira, A.K.V.; Aghaei, M.; Rüther, R. Automatic Inspection of Photovoltaic Power Plants Using. Aerial Infrared Thermography: A Review. *Energies* **2022**, *15*, 2055. [CrossRef]
35. Bommes, L.; Pickel, T.; Buerhop-Lutz, C.; Hauch, J.; Brabec, C.; Peters, I.M. Computer vision. tool for detection, mapping, and fault classification of photovoltaics modules in aerial IR videos. *Prog. Photovolt. Res. Appl.* **2021**, *29*, 1236–1251. [CrossRef]
36. Bommes, L.; Buerhop-Lutz, C.; Pickel, T.; Hauch, J.; Brabec, C.; Peters, I.M. Georeferencing of photovoltaic modules from aerial infrared videos using structure-from-motion. *Prog. Photovolt. Res. Appl.* **2022**, *30*, 1122–1135. [CrossRef]
37. Grimaccia, F.; Leva, S.; Dolara, A.; Aghaei, M. Survey on PV modules common faults after an O&M flight extensive campaign over different plants in Italy. *IEEE J. Photovolt.* **2017**, *7*, 810–816. [CrossRef]
38. Di Tommaso, A.; Betti, A.; Fontanelli, G.; Michelozzi, B. A multi-stage model based on YOLOv3 for defect detection in PV panels based on IR and visible imaging by unmanned aerial vehicle Renew. *Energy* **2022**, *193*, 941–962. [CrossRef]
39. Muttillo, M.; Nardi, I.; Stornelli, V.; de Rubeis, T.; Pasqualoni, G.; Ambrosini, D. On Field Infrared Thermography Sensing for PV System Efficiency Assessment: Results and Comparison with Electrical Models. *Sensors* **2020**, *20*, 1055. [CrossRef] [PubMed]
40. Amiri, A.F.; Oudira, H.; Chouder, A.; Kichou, S. Faults detection and diagnosis of PV systems based on machine learning approach using random forest classifier. *Energy Convers. Manag.* **2024**, *301*, 118076. [CrossRef]
41. Peng, H.; Cui, Y.; Bai, D.; Huang, Q.; Chen, X. A component-level defect detection and real-time localisation method for photovoltaic arrays using UAV-based infrared imagery. *Sensors* **2026**, *26*, 3736. [CrossRef] [PubMed]
42. Bontoș, M.D.; Vasiliu, G.-C.; Barbu, E.-L.; Boncescu, C.; Cocârță, D.M. A QGIS-Based Gaussian Plume Dispersion Model for Point Sources: Development and Intercomparison of Reflective and Non-Reflective Formulations. *Appl. Sci.* **2026**, *16*, 1833. [CrossRef]

Disclaimer/Publisher's Note: The statements, opinions and data contained in all publications are solely those of the individual author(s) and contributor(s) and not of MDPI and/or the editor(s). MDPI and/or the editor(s) disclaim responsibility for any injury to people or property resulting from any ideas, methods, instructions or products referred to in the content.